Analyzing and Characterizing Common Mode Chokes for Three Phase Systems

Álvaro Ojeda-Rodríguez, Carlos Domínguez-Palacios, Joaquín Bernal-Méndez, *Senior Member, IEEE*, and María A. Martín-Prats, *Senior Member, IEEE*

***Abstract*—Common mode chokes (CMCs) are widely employed to reduce common mode emissions of three phase systems. This work presents an advanced technique for analyzing and characterizing CMCs with three or four windings. The central idea of the method is a modal analysis of the choke, where the modes are based on the modes of the noise signal transmitted by the three-phase line. These modes are defined following the criterion of its suitability from the perspective of electromagnetic interference control. This modal analysis is used to propose a circuit model of the choke that accounts for the impact of high-frequency parasitic effects and, at the same time, allows for a straightforward parameter identification. This parameter identification is achieved by using a characterization technique that makes use of measurements of the response of the CMC in simple connections, whose suitability is justified thanks to the ability of the modal analysis to provide analytical and easy-to-interpret expressions of these connections. This makes also possible to predict and quantify mode conversions caused by the device in the three-phases line. The accuracy of the obtained circuit model within a wide frequency range has been demonstrated by comparing measurements with calculated responses for several three- and four-wires CMCs.**

***Index Terms*—Common mode choke (CMC), conducted emissions attenuation, conducted emissions propagation modes, high frequency circuit model, modal analysis, parasitic effects.**

I. Introduction

CURRENT trends in power electronics are toward the increase of switching frequencies and the power density of converters. An inevitable outcome of this tendency is the progressive increase of the electromagnetic emissions of power converters [1]. This poses a serious problem due to the necessity to comply with electromagnetic compatibility (EMC) regulations, which establish limits on the electromagnetic emissions of power converters in wide frequency ranges [2], [3], [4].

Manuscript received 1 August 2023; revised 10 October 2023 and 30 November 2023; accepted 21 January 2024. Date of publication 26 January 2024; date of current version 20 March 2024. This work was supported in part by the project TED2021-131954B-I00, funded by MCIN/AEI/10.13039/501100011033 and in part by the European Union "NextGenerationEU"/PRTR. Recommended for publication by Associate Editor Minjie Chen. *(Corresponding author: Álvaro Ojeda-Rodríguez.)*

Álvaro Ojeda-Rodríguez, Carlos Domínguez-Palacios, and María A. Martín-Prats are with the Department of Ingeniería Electrónica, Universidad de Sevilla, 41092 Sevilla, Spain (e-mail: aorodriguez@us.es; cdominguezpalacios@us.es; mmprats@us.es).

Joaquín Bernal-Méndez is with the Department of Física Aplicada III, Universidad de Sevilla, 41092 Sevilla, Spain (e-mail: jbmendez@us.es).

This article has supplementary material provided by the authors and color versions of one or more figures available at https://doi.org/10.1109/TPEL.2024.3359092.

Digital Object Identifier 10.1109/TPEL.2024.3359092

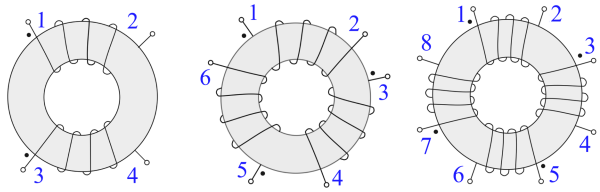

Fig. 1. Schematic representation of CMCs with different number of windings. (a) 2W-CMC. (b) 3W-CMC. (c) 4W-CMC.

Electromagnetic interference (EMI) filters are used to mitigate electromagnetic emissions of electronic equipment [5]. Among the components of EMI filters, common mode chokes (CMC), which are made up of two or more coupled coils wounded on a magnetic core, are widely employed due to its ability to reduce common mode (CM) emissions [5], [6].

Fig. 1 shows an sketch of a typical CMC used in one-phase systems. We will refer to this device as as two-wire CMC (2W-CMC). By contrast, three-phase systems can be implemented with either three-wire or four-wire conductors line [7], [8]. Consequently, CMCs used in three-phase systems are either three-wire CMCs (3W-CMCs) like that in Fig. 1(b), or four-wire CMCs (4W-CMCs) like that in Fig. 1(c) [8], [9].

In recent years, an important effort has been made to develop techniques for obtaining high-frequency circuit models of 2W-CMCs [10], [11], [12], [13], [14], [15], [16], [17], [18], [19]. However, much less works have been published dealing with the characterization of CMCs for three-phase applications or analyzing its effect on noise modes in the three-phase line [20]. The current trend in modern power electronics toward the increase of switching frequencies has been boosted by recent advances in semiconductor technologies and by the upsurge of applications, such as those related to transport electrification, where achieving high power density is a priority. This is expected to exacerbate EMC issues in modern three-phase systems [21], [22]. In this context, a method capable of providing accurate broadband models of 3W-CMCs and 4W-CMCs can help to develop virtual prototypes of EMI filters and/or complete systems. This can reduce the time and cost associated with trial and error design processes, thus allowing the development of EMC-compliant three-phase systems with high power densities [12], [15], [23]. Design methods for 3W-CMCs have already been presented in [21] and [24]. However, those methods are more focused on

the design of 3W-CMCs to comply with certain attenuation requirements than on characterizing a given sample. As a consequence, they concentrate on modeling the CM impedance of the 3W-CMC, and a differential mode (DM) model of the 3W-CMCs is not derived. Also, [12] reports a single example of application of a characterization method developed for 2W-CMCs to the case of a 3W-CMCs. However, the proposed circuit model is purely behavioral and the characterization technique is based on a more complex set of measurements. A simpler characterization method for 3W-CMCs, requiring only a measurement with a quite simple setup, has been presented by Dominguez-Palacios et al. [25]. However, this method has a limited accuracy due to a nonprecise characterization of the effect of intrawinding coupling. Also, in that work, no complete modal theory is provided that can account for the response of the 3W-CMC in different connections and explain its effect on the modes of the line. In addition, the works cited above do not deal with 4W-CMCs. As we will see, the 4W-CMC case has particularities that do not allow us to treat it as a straightforward generalization of the 3W-CMC case.

In this work, accurate wideband circuit models and a simple characterization technique are proposed for both 3W-CMCs and 4W-CMCs. The ideas, concepts, and experimental techniques developed in this work are supported by a modal analysis that allows a significant simplification of the analysis of the response of 3W- and 4W-CMCs, facilitating their characterization. To carry out this analysis, we start by defining a mode decomposition for signals in three-phase transmission lines (with three or four wires) that is convenient from an EMC perspective. We demonstrate that, given these modes, the condition that ensures that a 3W-CMC or a 4W-CMC does not cause conversion between modes is that the circuit model of the CMC has a set of natural modes that are derived from those defined in the line. We propose equivalent circuits for 3W-CMCs and 4W-CMCs that model them as six- or eight-port networks consisting of *LCR* resonant tanks with both magnetic and electrical coupling between them. It is shown that, under the reasonable assumption that the electrical couplings between coils are equal, the 3W-CMCs do not cause conversion between the modes defined in three-wire transmission lines. By contrast, the fact that the magnetic couplings between nearby and distant coils are different in 4W-CMCs causes conversion between the so-called differential and homopolar modes in four-wire lines. Moreover, we demonstrate that, for both 3W-CMCs and 4W-CMCs, it is possible to construct an alternative circuit model, derived from that originally proposed, that has the additional advantage that its parameters are grouped into blocks so that each block is associated with only one of the natural modes of the circuit. This allows for an easy assignment of values to the parameters of the model. To that end, we propose to use an advanced search algorithm that takes as input the measurements of a pair of transmission coefficients of the CMC in two simple setups, which reveal all the modal responses of the CMC. To demonstrate the suitability of the proposed circuit models and characterization method, we have characterized and verified a wide range of 3W- and 4W-CMCs. Mode conversion caused by 4W-CMCs with symmetrically distributed windings around the core has also been experimentally verified.

TABLE I
DEFINITION OF NOISE PROPAGATION MODES

	Name	Voltage mode
COMMON MODES	CM1	$v_1 = [+1, +1, +1, +1]$
	CM2	$v_2 = [+1, +1, +1, -3]$
DIFFERENTIAL MODES	DM1	$v_3 = [+1, +1, -2, 0]$
	DM2	$v_4 = [+1, -1, 0, 0]$

The rest of this article is organized as follows. Section II presents and justifies a convenient definition of modes for a noise signal propagating in a 3-wire or 4-wire three-phase line. Section III proposes high-frequency circuit models for 3W- and 4W-CMCs and presents the key ideas of a generalized modal analysis that facilitates analysis of the problem and identification of the elements of the circuit models. Section IV outlines a particularly simple technique to find the value of the parameters of the circuit models of the CMCs. A method to validate the equivalent circuit models of 3W- and 4W-CMCs is presented in Section V. Section VI is devoted to presenting several examples to demonstrate the precision and evaluate the scope of the characterization technique for 3W- and 4W-CMCs proposed in this work. Finally, Section VII concludes this article. In addition, in Appendix A, a mathematical demonstration is provided for a result with high relevance in the context of this work.

II. NOISE MODES DEFINITION

Three-phase power lines can be regarded as $(N+1)$-conductors transmission lines with $N = 3$, or $N = 4$ if neutral conductor is present [26]. By comparison, single-phase transmission lines (with $N = 2$) support in general two propagation modes. In the analysis of conducted emissions in single-phase systems, they are typically decomposed into CM and DM. This is done for convenience, as CM and DM typically have different generation mechanisms, give rise to different electromagnetic compatibility issues (e.g., CM emissions tend to more easily create coupling problems and radiated emissions), and require specific attenuation techniques [5]. Therefore, it is reasonable to apply the same criteria in determining which propagation modes should be defined in three-phase systems.

Distinction between CM and DM in three-phase systems has been carried out in several previous works, mostly in three-wire systems [20], [27], [28]. In a few studies, this decomposition is performed in four-wire lines, but exclusively to study the behavior of CM, whose definition may vary [29], [30]. In summary, an agreement cannot be found in the literature on the more convenient definition, from an EMC perspective, of propagation modes for three-phase systems. To address this problem, in this work, we propose the decomposition of the signal in a four-wire line according to the modes shown in Table I. The currents associated with each mode are shown in Fig. 2. The idea behind this decomposition is to obtain a decomposition of the signal on

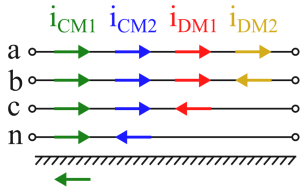

Fig. 2. Representation of noise propagation modes defined in this work for four-wire three phase systems.

the line into two modes unrelated to the functional currents of the system, labeled as CMs (CM1 and CM2) in Table I, and another two modes, identified as DMs (DM1 and DM2), which account for the (low-frequency) power currents that must flow through the line. The CM1 and CM2 modes in Table I are identified as CM because they imply a nonzero net current flowing in the three power lines (lines a, b, and c in Fig. 2). In fact, CM1 is a true CM for the four-wires line, whereas CM2 stands for a homopolar or zero-sequence component of the three-phase current. These modes CM1 and CM2 are similar to CM defined in single-phase lines in that they have specific generation mechanisms in power electronics devices attached to the power line, which are typically related to the presence of parasitic capacitances in nodes with rapid voltage variations [5]. In addition, these CM modes can easily give rise to coupling and radiation problems and must be attenuated using specific techniques, including the use of CMCs. The modal decomposition shown in Table I is an extension to four wires of the proposal reported in [20], [28] for three-wire systems. From a mathematical point of view, it is more convenient to normalize the orthogonal voltage vectors in Table I so that they all have a unit magnitude. This normalization leads to the following transformation matrix:

$$\boldsymbol{T}_{\mathbf{4W}} = \begin{bmatrix} \frac{1}{2} & \frac{1}{2\sqrt{3}} & \frac{1}{\sqrt{6}} & \frac{1}{\sqrt{2}} \\ \frac{1}{2} & \frac{1}{2\sqrt{3}} & \frac{1}{\sqrt{6}} & \frac{-1}{\sqrt{2}} \\ \frac{1}{2} & \frac{1}{2\sqrt{3}} & \frac{-2}{\sqrt{6}} & 0 \\ \frac{1}{2} & \frac{-3}{2\sqrt{3}} & 0 & 0 \end{bmatrix} \tag{1}$$

This modal decomposition coincides with the natural modes of a sufficiently symmetric four-wires line [26]. Note that the columns in $\boldsymbol{T}_{\mathbf{4W}}$ are the normalized CM1, CM2, DM1, and DM2 modes defined in Table I. Thus, $\boldsymbol{T}_{\mathbf{4W}}$ represents the matrix of change of basis between the (normalized) modes defined in Table I and the ordinary basis of the line.

The modal decomposition given in (1) can be readily particularized for a three-wire transmission line by using the following transformation matrix:

$$\boldsymbol{T}_{\mathbf{3W}} = \begin{bmatrix} \frac{1}{\sqrt{3}} & \frac{1}{\sqrt{6}} & \frac{1}{\sqrt{2}} \\ \frac{1}{\sqrt{3}} & \frac{1}{\sqrt{6}} & \frac{-1}{\sqrt{2}} \\ \frac{1}{\sqrt{3}} & \frac{-2}{\sqrt{6}} & 0 \end{bmatrix} \tag{2}$$

This 3×3 transformation matrix can be obtained simply by eliminating the first column and the last row of $\boldsymbol{T}_{\mathbf{4W}}$ in (1) and performing a convenient renormalization of the column vectors. Note that the modal decomposition given by $\boldsymbol{T}_{\mathbf{3W}}$ in (2) corresponds of the Clarke or alpha-beta transformation commonly used in three-phase systems [31], [32]. From an EMC perspective, the first column in $\boldsymbol{T}_{\mathbf{3W}}$ corresponds to a CM, and the other two columns are the DMs that account for the functional currents that are expected to flow in the line.

III. Modal Analysis and HF Circuit Model

In general, a CMC or any other filtering device inserted in a $N+1$-conductors transmission line should be regarded as a $2N$-ports passive network. In single-phase systems, the effect of the CMC is analyzed by studying the insertion loss for each mode (CM and DM) of the line [5]. However, asymmetries in the filtering device can result in energy transfer between modes [33]. Regarding this, Ojeda-Rodríguez et al. [19] demonstrated that the condition for a 2W-CMC not to cause undesired mode conversion between CM and DM in a single-phase transmission line translates into a necessary and sufficient condition for the four natural modes (eigenvectors of the admittance matrix) of the 2W-CMC. Therefore, a pertinent question is whether, for a set of N propagation modes, such as that defined in the previous section for a three-phase transmission line, there also exists a set of $2N$ natural modes of the CMC that ensures that the device will cause no mode conversion in the line. The answer to this question is provided in Appendix A, where it is demonstrated that for a set of N transmission modes selected in an $N+1$-conductors line and organized as columns vectors of an $N \times N$ matrix ($\boldsymbol{T}$), the condition that a passive device with input–output symmetry (such as a CMC) inserted into that line must satisfy in order to avoid mode conversion between those N transmission modes is that the $2N$ natural modes of its $2N$-ports circuit model can be arranged as column vectors of a $2N \times 2N$ matrix ($\boldsymbol{E}$), which can be expressed in terms of $\boldsymbol{T}$ submatrices as follows:

$$\boldsymbol{E} = \begin{bmatrix} \boldsymbol{T} & \boldsymbol{T} \\ \boldsymbol{T} & -\boldsymbol{T} \end{bmatrix}. \tag{3}$$

Therefore, $\boldsymbol{E}$ in (3) establishes the necessary relationship that must exist between the N propagation modes of the line and the $2N$ natural modes of the CMC (or any other $2N$-ports device inserted in the line) that ensures no mode conversion among these N propagation modes on the line.

A. Circuit Model for a 3W-CMC

Essentially, a 3W-CMC consists of three tightly coupled coils, and its objective is to attenuate the propagation of the CM on the three-wire line without causing conversion between this mode and the DMs that can propagate in the line. This is achieved in principle by a simple arrangement consisting of three equal coils with a strong mutual coupling between them. However, parasitic capacitances between turns cause each of these coils to behave actually as parallel *LCR* resonators [11], [12], [17]. In addition, electrical coupling between different coils must be

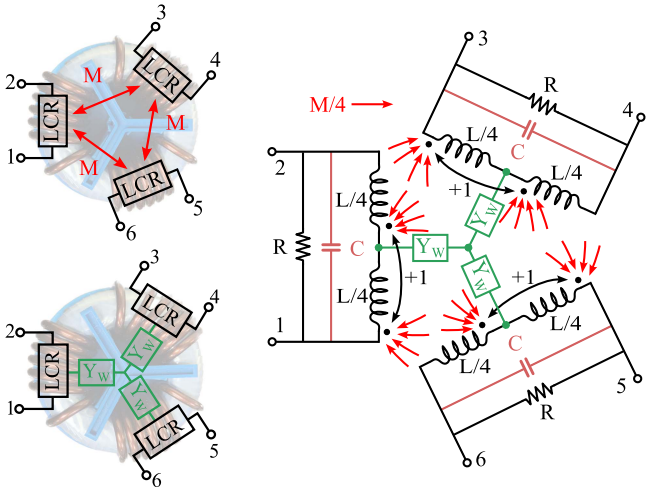

Fig. 3. Circuit model for the 3W-CMC with three evenly distributed windings. Each winding is modeled by a LCR resonant circuit. M and Y_{W} account for the magnetic and electric couplings between windings, respectively.

TABLE II
MODES OF A SIX-PORTS NETWORK (3W-CMC) ENSURING NO MODE CONVERSION BETWEEN MODES DEFINED IN A THREE-WIRES LINE

Name	Voltage mode
Ground (G)	$v_{\mathrm{G}} = [+1, +1, +1, +1, +1, +1]$
Intrawinding 1 (W1)	$v_{\mathrm{W1}} = [+1, +1, +1, +1, -2, -2]$
Intrawinding 2 (W2)	$v_{\mathrm{W2}} = [+1, +1, -1, -1, 0, 0]$
Common (C)	$v_{\mathrm{C}} = [+1, -1, +1, -1, +1, -1]$
Differential 1 (D1)	$v_{\mathrm{D1}} = [+1, -1, +1, -1, -2, +2]$
Differential 2 (D2)	$v_{\mathrm{D2}} = [+1, -1, -1, +1, 0, 0]$

accounted for in order to achieve a wideband circuit model [11]. Those effects are schematically represented in Fig. 3. This figure also includes a proposed circuit model for the 3W-CMC, which is a six-ports network thoroughly devised to account for these high frequency effects and, at the same time, to ensure that the 3W-CMC does not cause mode conversion of the modes defined in (2) for three-wire transmission lines, which is a desirable characteristic of practical 3W-CMCs.

To demonstrate that the circuit model of the 3W-CMC in Fig. 3 will not give rise to mode conversion between the propagation modes on the three-wire lines defined by $\boldsymbol{T}_{\mathbf{3W}}$ in (2) it is enough to verify that the eigenvectors of the admittance matrix of that six-ports network coincides with those listed in Table II, which are obtained by applying the splitting shown in (3) to the set of modes defined by $\boldsymbol{T}_{\mathbf{3W}}$. Note that the voltage modes in Table II are not normalized to make them easier to read and interpret. It is interesting to note that the first three modes in Table II (i.e. modes G, W1, and W2) produce equal excitations at both terminals of each coil. Therefore, these modes account for the capacitive responses of the 3W-CMC. On the other hand, modes C, D1, and D2 in Table II involve a voltage drop between the terminals of the inductances of the 3W-CMC. However, while the C mode will generate CM currents that sum their magnetic

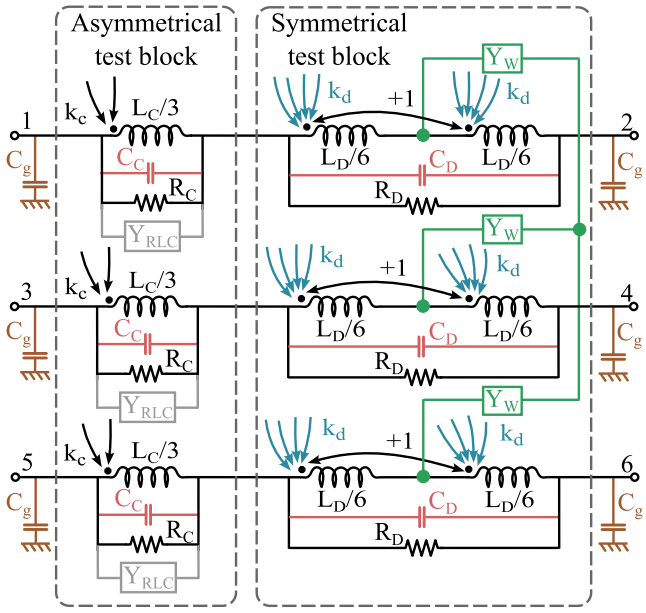

Fig. 4. Modal-parameters circuit (MPC) model for the 3W-CMC.

fluxes in the core of the 3W-CMC, modes D1 and D2 will result in differential currents in the 3W-CMC, i.e., currents whose net magnetic flux in the core of the 3W-CMC would be nearly zero.

Note that all the elements of the circuit model in Fig. 3 have a clear physical meaning. However, this circuit model does not comply with additional requirements, which would also be highly desirable. That is, that the parameters of the circuit model can be independently associated with the modal admittances (eigenvalues of the admittance matrix) of the 3W-CMC. This feature is essential because it greatly simplifies the extraction of parameters for the circuit model of the 3W-CMC, as demonstrated in [19] for the case of 2W-CMCs. In that work, the proposed circuit model for 2W-CMCs is referred to as the modal parameters circuit (MPC) of the 2W-CMC. Therefore, the question immediately arises whether it is possible to modify the circuit in Fig. 3 to construct an MPC model for 3W-CMCs.

Fig. 4 shows a MPC model of a 3W-CMC that is completely equivalent to that in Fig. 3. The components of the MPC model of the 3W-CMC in Fig. 4 are arranged in two blocks: asymmetrical mode test block (left) and symmetrical mode test block (right). Asymmetrical mode test block is made up of three perfectly-coupled windings ($k_c = 1$), each one modeled by the inductance $L_{\mathrm{C}}/3$, where $L_{\mathrm{C}} = L + 2\,M$ is the inductance seen by the CM current. The typical resonant behavior of these coils is accounted for by the parallel C_{C} and R_{C} elements. Also, the Y_{RLC} admittance in the asymmetrical mode test block, consisting of one or more parallel RC and/or RL branches, is intended to take into account the effects of either magnetic losses or dielectric losses, as explained in [19]. Note that, due to the perfect coupling between coils in the asymmetrical mode test block, this block will be short-circuited by current modes other than C. On the other hand, symmetrical mode test block is made up of three pairs of inductances $L_{\mathrm{D}}/6$ coupled as indicated in Fig. 4, being $k_d = 1$ and $L_{\mathrm{D}} = L - M$, where L_{D} is the inductance seen by

TABLE III
MODAL ADMITTANCES OF THE MPC MODEL OF A 3W-CMC IN FIG. 4

Mode	Modal admittance
G	$Y_{\mathrm{G}} = j\omega C_g \simeq 0$
W1, W2	$Y_{\mathrm{W}} = \dfrac{1}{2\left(\dfrac{1}{j\omega C_{\mathrm{W}}} + \dfrac{1}{Y_{\mathrm{LCR_W}}}\right)}$
C	$Y_{\mathrm{C}} = 2\left(j\omega C_{\mathrm{C}} + \dfrac{1}{j\omega L_{\mathrm{C}}} + \dfrac{1}{R_{\mathrm{C}}} + Y_{\mathrm{RLC}}\right)$
D1, D2	$Y_{\mathrm{D}} = 2\left(j\omega C_{\mathrm{D}} + \dfrac{1}{j\omega L_{\mathrm{D}}} + \dfrac{1}{R_{\mathrm{D}}}\right)$

differential currents. It can be checked that this coupling forces inductances of the symmetrical mode block to be short-circuited by both common (C) and intra-windings (W1, W2) modes. In this block, C_{D} models the capacitive behavior of the windings at high frequencies when excited with DMs D1 and D2, whereas Y_{W} determines the response of the 3W-CMC when excited with intra-windings modes W1 and W2. This Y_{W} admittance will be, in principle, that of a simple C_{W} inter-winding capacitance. However, if necessary, the Y_{W} admittance can also integrate a LCR_{W} network (a parallel LCR tank) in series with the C_{W} inter-winding capacitance. As explained in [19], this resonant tank accounts for inter-turns resonances, which arise in some cases at sufficiently high frequencies due to the fact that the wavelength inside a core with high permeability and high permittivity may become quite small [34]. Finally, it should be noted that although a parasitic capacitance between each single terminal and ground C_{g} is included in Fig. 4, its effect can be neglected in this analysis for the same reasons as explained in [19].

It can be easily checked that the eigenvectors of the admittance matrix of the 3W-CMC MPC circuit model in Fig. 4 are those listed in Table II. A first hint of the suitability of the proposed circuit model comes from the simplicity of the corresponding eigenvalues or modal admittances, which are given in Table III. Moreover, note that none of the parameters of the model is involved in more than one modal admittance. This is a key feature of the proposed MPC model that, along with the simple measurement setups that will be presented in Section IV, facilitates the efficient determination of its parameters.

B. Circuit Model for a 4W-CMC

Fig. 5 shows the main physical effects that should be modeled for a 4W-CMC manufactured with a toroidal core and four evenly distributed windings on it. In principle, the circuit model in Fig. 5 is a direct extension of the 3W-CMC case to include one more LCR resonant circuit. However, a key difference between 4W-CMCs and 3W-CMCs is that in the latter case the relative position of each two windings in the core is the same, which allows us to assume that both magnetic and electric couplings between windings are the same for every pair of windings. However, a 4W-CMC has two different relative positions between

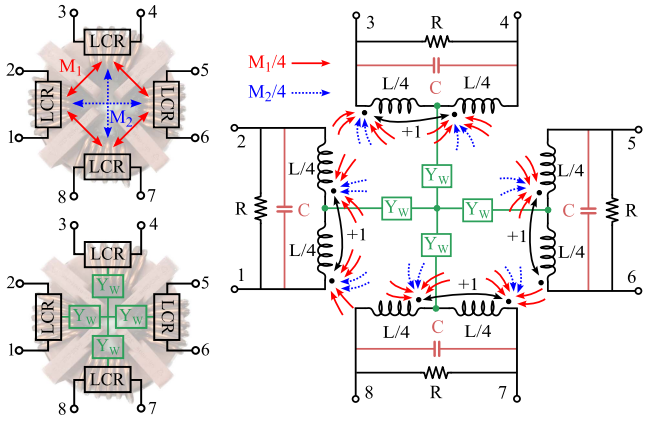

Fig. 5. Circuit model for the 4W-CMC with four windings evenly distributed. Each winding is modeled by an LCR resonant circuit. M_1 and M_2 account for the magnetic coupling between nearby and distant windings respectively. The admittance Y_{W} accounts for the electric coupling between windings.

each pair of windings: either they are nearby windings or they are distant windings, i.e., placed at opposite sides of the ring core. For this reason, in the 4W-CMC model we will assume that the magnetic couplings between nearby coils are greater than between distant coils, i.e. $M_1 > M_2$. This difference in the magnetic couplings of different pairs of coils wound in the same core has been previously pointed out in [35], and it should be caused by the fact that the number of magnetic field lines linking both windings depends on the relative position of both windings in the core [6]. This effect will be experimentally verified for 4W-CMCs with symmetrically arranged windings in Section VI. In this section, its relevant practical consequences will be analyzed.

Unlike magnetic couplings, the electric couplings between each pair of coils are assumed to be the same in the circuit model proposed in Fig. 5. This is justified by the fact that most core materials, for example MnZn or nanocrystalline cores, have extremely large electric permittivities [22], [34]. This results in strong electric couplings between the windings which is associated with the electric field that connects both windings through the core [18], [22]. Since a change in the relative position between two windings on a toroidal core implies that the distance between them increases on one side but decreases on the opposite side, the relative position of the two windings has little effect on the parasitic capacitance between them. This has been experimentally tested in [18], and we double checked it by measuring parasitic capacitances between different windings in 4W-CMCs with different core materials. Additional verification is provided by the good results provided systematically by the proposed circuit model to characterize a great number of different CMCs, as we will see in Section VI.

1) Mode Conversion in 4W-CMCs: In this section we will demonstrate that the difference between the mutual inductances of nearby and distant coils in the circuit model in Fig. 5 causes mode conversion between some of the modes defined for a four-wires line in Table I.

TABLE IV
MODES OF A EIGHT-PORTS NETWORK (4W-CMC) ENSURING NO MODE CONVERSION BETWEEN MODES DEFINED IN A FOUR-WIRES LINE

Name	Voltage mode
Ground (G)	$v_{\mathrm{G}} = [+1,+1,+1,+1,+1,+1,+1,+1]$
Intra-winding 1 (W1)	$v_{\mathrm{W1}} = [+1,+1,+1,+1,+1,+1,-3,-3]$
Intra-winding 2 (W2)	$v_{\mathrm{W2}} = [+1,+1,+1,+1,-2,-2,0,0]$
Intra-winding 3 (W3)	$v_{\mathrm{W2}} = [+1,+1,-1,-1,0,0,0,0]$
Common (C)	$v_{\mathrm{C}} = [+1,-1,+1,-1,+1,-1,+1,-1]$
Homopolar (H)	$v_{\mathrm{H}} = [+1,-1,+1,-1,+1,-1,-3,+3]$
Differential 1 (D1)	$v_{\mathrm{D1}} = [+1,-1,+1,-1,-2,+2,0,0]$
Differential 2 (D2)	$v_{\mathrm{D2}} = [+1,-1,-1,+1,0,0,0,0]$

According to the demonstration presented in appendix A, the condition to ensure that the 4W-CMC does not cause mode conversion between the line modes in Table I, is that the eigenvectors of the 8×8 admittance matrix of its circuit model, $\boldsymbol{Y_{4W}}$, are the columns of the following matrix:

$$\boldsymbol{E_{4W}} = \begin{bmatrix} \boldsymbol{T_{4W}} & \boldsymbol{T_{4W}} \\ \boldsymbol{T_{4W}} & -\boldsymbol{T_{4W}} \end{bmatrix} \tag{4}$$

where $\boldsymbol{T_{4W}}$ is defined in (1). The non-normalized voltage excitations defined by the columns of $\boldsymbol{E_{4W}}$ are represented in Table IV. The first four rows in Table IV define excitations with the same voltage imposed at the two terminals of each winding and, therefore, are expected to give rise to a capacitive response of the device mainly associated with electrical coupling between windings. By contrast, the last four rows of Table IV correspond to voltage excitation where the windings are excited either in CM, in homopolar mode or in two additional DMs referred to here as D1 and D2. Note that if these modes happen to be eigenvectors of the admittance matrix of the 4W-CMC, each of them will give rise to currents directly proportional to the voltage excitation represented by its eigenvector. Therefore, referring to the line modes in Table I, excitation of the 4W-CMC in mode C will result in a CM1 mode in the line, whereas excitation in mode H will result in a CM2 mode propagating in the four-wires line, which is regarded as a zero-sequence or homopolar mode. This homopolar mode is a CM with respect to the three power lines (i.e., leaving the neutral cable out) but it is a DM with respect to the four wires because the sum of the excitations on these wires is zero. On the other hand, note that D1 and D2 are DMs with respect to either the three power lines or the four wires. As explained previously, D1 and D2 should be components of the functional currents of a three-phase device, which makes them equivalent to the DM defined in single-phase systems.

A convenient way to analyze mode conversion in the 4W-CMC is to represent its admittance matrix $\boldsymbol{Y_{4W}}$ on the basis given by $\boldsymbol{E_{4W}}$. In the case of the circuit model proposed in Fig. 5, this change of basis leads to the following result:

$$\boldsymbol{Y_{4WE}} = \boldsymbol{E_{4W}^{-1}} \boldsymbol{Y_{4W}} \boldsymbol{E_{4W}} = \begin{bmatrix} \boldsymbol{Y_{UP}} & \boldsymbol{0} \\ \boldsymbol{0} & \boldsymbol{Y_{DW}} \end{bmatrix} \tag{5}$$

Where $\boldsymbol{0}$ stand for a 4×4 zero matrix and $\boldsymbol{Y_{UP}}$ is a diagonal 4×4 matrix that can be written as follows:

$$\boldsymbol{Y_{UP}} = \begin{bmatrix} Y_{\mathrm{G}} & 0 & 0 & 0 \\ 0 & Y_{\mathrm{W}} & 0 & 0 \\ 0 & 0 & Y_{\mathrm{W}} & 0 \\ 0 & 0 & 0 & Y_{\mathrm{W}} \end{bmatrix} \tag{6}$$

where Y_{G} and Y_{W} are capacitive admittances that account for electric couplings to the ground and between coils. On the other hand, $\boldsymbol{Y_{DW}}$ is another 4×4 matrix that has the following form:

$$\boldsymbol{Y_{DW}} = \begin{bmatrix} Y_{\mathrm{C}} & 0 & 0 & 0 \\ 0 & \frac{Y_{\mathrm{DN1}}+2Y_{\mathrm{DN2}}}{3} & \frac{Y_{\mathrm{DN2}}-Y_{\mathrm{DN1}}}{3\sqrt{2}} & \frac{Y_{\mathrm{DN1}}-Y_{\mathrm{DN2}}}{\sqrt{6}} \\ 0 & \frac{Y_{\mathrm{DN2}}-Y_{\mathrm{DN1}}}{3\sqrt{2}} & \frac{Y_{\mathrm{DN1}}+5Y_{\mathrm{DN2}}}{6} & \frac{Y_{\mathrm{DN2}}-Y_{\mathrm{DN1}}}{3\sqrt{2}} \\ 0 & \frac{Y_{\mathrm{DN1}}-Y_{\mathrm{DN2}}}{\sqrt{6}} & \frac{Y_{\mathrm{DN2}}-Y_{\mathrm{DN1}}}{3\sqrt{2}} & \frac{Y_{\mathrm{DN1}}+Y_{\mathrm{DN2}}}{2} \end{bmatrix} \tag{7}$$

where Y_{C}, Y_{DN1}, and Y_{DN2} are the eigenvalues associated with the four resonant modes (or eigenvectors) of the system of four magnetically coupled resonators that made up the 4W-CMC. Those resonant modes are illustrated in Fig. 6. It can be easily demonstrated that for four equal LCR resonators, those eigenvalues can be expressed as:

$$Y_{\mathrm{C}} = 2\left(j\omega C_{\mathrm{C}} + \frac{1}{j\omega L_{\mathrm{C}}} + \frac{1}{R_{\mathrm{C}}}\right) \tag{8a}$$

$$Y_{\mathrm{DN1}} = 2\left(j\omega C_{\mathrm{D}} + \frac{1}{j\omega L_{\mathrm{D1}}} + \frac{1}{R_{\mathrm{D1}}}\right) \tag{8b}$$

$$Y_{\mathrm{DN3}} = Y_{\mathrm{DN2}} = 2\left(j\omega C_{\mathrm{D}} + \frac{1}{j\omega L_{\mathrm{D2}}} + \frac{1}{R_{\mathrm{D2}}}\right) \tag{8c}$$

where in principle, $R_{\mathrm{C}} = R_{\mathrm{D1}} = R_{\mathrm{D2}}$ and $C_{\mathrm{C}} = C_{\mathrm{D}}$ are the resistance and capacitance of the four equal resonators. We use here different subscripts for convenience, since the circuit model that will be presented in the next section will allow us to independently fix these parameters. Note that there is no difference between DN2 and DN3 modes from a physical point of view, since they provoke the same response of the 4W-CMC. From a mathematical point of view, they are linearly independent eigenvectors of the admittance matrix with the same eigenvalue (degenerate eigenvectors).

Note that the matrix $\boldsymbol{Y_{DW}}$ in (7) is not in general a diagonal matrix unless $Y_{\mathrm{DN1}} = Y_{\mathrm{DN2}}$ (i.e., $M_1 = M_2$). Therefore, $\boldsymbol{Y_{4WE}}$ in (5) is not in general diagonal. In fact, the distribution of the elements of $\boldsymbol{Y_{4WE}}$ reveals that the main effect of the inequality of mutual couplings between nearby and distant windings in a 4W-CMC is that, when inserted in a four-wires line, the 4W-CMC will cause mode conversion between the homopolar mode (CM2 in Table I) and the two DMs (DM1 and DM2) of the line. On the other hand, the fact that Y_{C} is the only nonzero element in its row and column in $\boldsymbol{Y_{4WE}}$ indicates that the 4W-CMC can provide attenuation to the CM (CM1 mode in Table I) without causing mode conversion with the rest of the modes of the line.

In summary, the problem of mode conversion in 4W-CMC can be understood by considering that the C, DN1, DN2 and

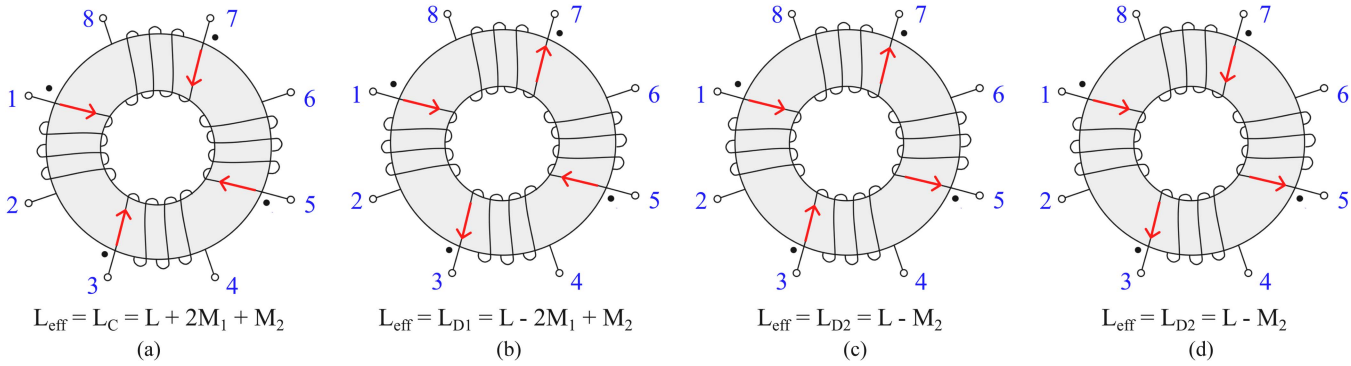

Fig. 6. Representation of the four natural modes of four magnetically coupled LCR resonators with different mutual inductances between nearby windings and distant windings (M_1 and M_2). The effective inductances seen for each mode at the terminals of the windings of the 4W-CMC are indicated below.

DN3 modes represented in Fig. 6 are the four noncapacitive natural modes for a 4W-CMC with $M_1 \neq M_2$. However, this set of modes is different from the noncapacitive modes (C, H, D1, and D2) listed in Table IV, which have been defined in (4) based on the criterion of their suitability from the EMC perspective. In particular, note that whereas C mode is present in both mode sets and, therefore, it is a natural mode of the 4W-CMC, the H, D1, and D2 modes in Table IV are not natural modes of the 4W-CMC unless $M_1 = M_2$. From a practical point of view, this implies that the presence of the 4W-CMC in the three-phases line can give rise to a homopolar (H) noise component due to mode conversion from DMs noise and vice versa.

2) MPC Circuit Model for a 4W-CMC: In this section, we demonstrate that it is possible to find a MPC model for a 4W-CMC, in a similar fashion as those found for 2W-CMCs in [19] and for 3W-CMCs in Section III-A. This MPC model should be equivalent to that in Fig. 5, but must be made up of independent circuit blocks, each one accounting for the response of the CMC to only one of the distinct modes listed in Table IV.

A careful analysis and decomposition of the circuit model in Fig. 5 leads to the MPC circuit model of the 4W-CMC shown in Fig. 7. Once again, this MPC circuit model features two main blocks. The asymmetrical mode test block is made up of four magnetically and perfectly coupled ($k_c = 1$) *LCR* resonant circuits, so that these components are responsible for the response of the 4W-CMC to asymmetrical mode test excitation exclusively. Therefore, this block causes no effect in differential currents and currents from one winding to another through interwinding capacitances. The inductance of each winding is the inductance seen by a CM current, $L_C = L + 2M_1 + M_2$. The role of admittance Y_{RLC} in this block is explained in Section III-A. As for the symmetrical mode test block, it is made up of two groups of four resonant circuits that are short-circuited by currents in C mode, and therefore account for the response of the 4W-CMC to differential excitations, and it also includes Y_W that accounts for the electric coupling between windings. Regarding the resonators, the first group of them features four perfectly coupled inductances ($k_{d1} = 1$), and it accounts for the resonance associated with the component of the DM current in the DN1 mode illustrated in Fig. 6(b). Therefore, this component of the DM current sees an inductance $L_{D1} = L - 2M_1 + M_2$

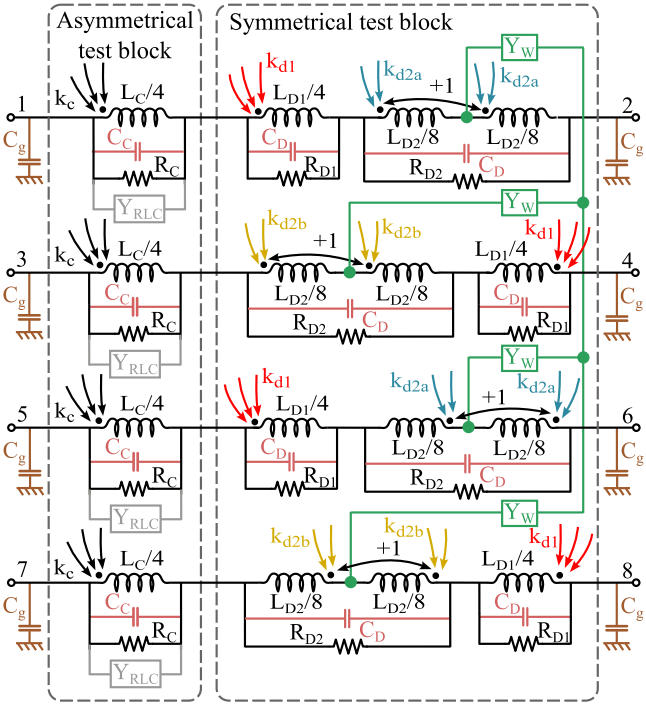

Fig. 7. Modal-parameters circuit (MPC) model for a 4W-CMC.

at low frequencies and a capacitance C_D after resonance. In addition, this group of resonators is short-circuited by the current modes DN2 and DN3 illustrated in Fig. 6(c) and (d). The second group of resonators within this symmetrical test block, characterized by $L_{D2} = L - M_2$, C_D and R_{D2} is designed to be short-circuited by both C mode currents and the DN1 mode currents represented in Fig. 6(b). For this reason, distant inductances are perfectly coupled ($k_{d2a} = k_{d2b} = 1$). All the resonators that belong to the symmetrical mode block are short-circuited by any of the intra-winding modes (W1, W2 and W3) too. Moreover, the inductances of this second group of resonators are split to provide a connection point for the intrawinding admittance Y_W. This admittance is excited exclusively by the intrawinding modes W1, W2, and W3, which short-circuit all the resonant tanks in the circuit. Table V lists the elements of the main

TABLE V
DIAGONAL ELEMENTS OF MATRIX $\boldsymbol{Y_{4WE}}$ IN (5) FOR THE MPC MODEL OF A 4W-CMC IN FIG. 7

Name	Admittance
G	$Y_{\mathrm{G}} = j\omega C_g \simeq 0$
W1, W2, W3	$Y_{\mathrm{W}} = \dfrac{1}{2\left(\dfrac{1}{j\omega C_{\mathrm{W}}} + \dfrac{1}{Y_{\mathrm{LCR_W}}}\right)}$
C	$Y_{\mathrm{C}} = 2\left(j\omega C_{\mathrm{C}} + \dfrac{1}{j\omega L_{\mathrm{C}}} + \dfrac{1}{R_{\mathrm{C}}} + Y_{\mathrm{RLC}}\right)$
H	$Y_{\mathrm{H}} = \dfrac{1}{3}Y_{\mathrm{DN1}} + \dfrac{2}{3}Y_{\mathrm{DN2}}$ $= 2j\omega C_{\mathrm{D}} + \dfrac{2}{3j\omega}\left(\dfrac{1}{L_{\mathrm{D1}}} + \dfrac{2}{L_{\mathrm{D2}}}\right) + \dfrac{2}{3}\left(\dfrac{1}{R_{\mathrm{D1}}} + \dfrac{2}{R_{\mathrm{D2}}}\right)$
D1	$Y_{\mathrm{D1}} = \dfrac{1}{6}Y_{\mathrm{DN1}} + \dfrac{5}{6}Y_{\mathrm{DN2}}$ $= 2j\omega C_{\mathrm{D}} + \dfrac{1}{3j\omega}\left(\dfrac{1}{L_{\mathrm{D1}}} + \dfrac{5}{L_{\mathrm{D2}}}\right) + \dfrac{1}{3}\left(\dfrac{1}{R_{\mathrm{D1}}} + \dfrac{5}{R_{\mathrm{D2}}}\right)$
D2	$Y_{\mathrm{D2}} = \dfrac{1}{2}Y_{\mathrm{DN1}} + \dfrac{1}{2}Y_{\mathrm{DN2}}$ $= 2j\omega C_{\mathrm{D}} + \dfrac{1}{j\omega}\left(\dfrac{1}{L_{\mathrm{D1}}} + \dfrac{1}{L_{\mathrm{D2}}}\right) + \left(\dfrac{1}{R_{\mathrm{D1}}} + \dfrac{1}{R_{\mathrm{D2}}}\right)$

diagonal of $\boldsymbol{Y_{4WE}}$ in terms of the components of the MPC model in Fig. 7.

In summary, the MPC circuit model of the 4W-CMC in Fig. 7 offers greater flexibility and independence of its parameters at the cost of slightly increased complexity compared to its equivalent circuit in Fig. 5. The main purpose of this trade-off is to significantly facilitate the process of determining the circuit's parameters and, consequently, improve the accuracy of the characterization of the 4W-CMC.

IV. CHARACTERIZATION TECHNIQUE

The procedure proposed in this work to obtain a numerical estimate of the parameters of the MPC model for the 3W- and 4W-CMC is based on simple measurements along with the use of an advanced search algorithm. Since this approach is very similar to that already proposed in [19], we will only outline it here for the sake of brevity. The proposed characterization technique has followingtwo main steps:

A. Step 1

First, the response of the CMC is measured in two quite simple connections which are referred to as open circuit (OC) connection, shown in Fig. 8, and the intrawinding (WD) connection, shown in Fig. 9. Apart from their simplicity, the key feature that makes these two connections specially suitable for characterizing the CMC is the fact that they explicitly reveal all the modal responses of the CMC. To demonstrate this, (9) and (10) show the transmission coefficients of the 3W-CMC and 4W-CMC in those two setups calculated in terms of modal admittances

$$S_{21}^{\mathrm{OC}} = \frac{3RY_{\mathrm{C}}Y_{\mathrm{D}}}{Y_{\mathrm{D}} + Y_{\mathrm{C}}\left(2 + 3RY_{\mathrm{D}}\right)} \tag{9a}$$

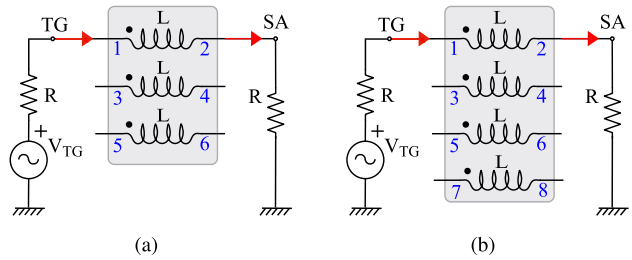

Fig. 8. Open circuit (OC) connection. (a) 3W-CMC. (b) 4W-CMC. In these schematics TG stands for tracking generator, and SA stands for spectrum analyzer.

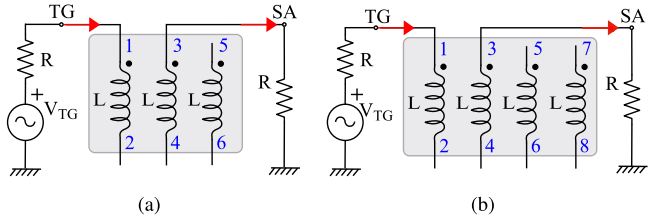

Fig. 9. Capacitive intra-winding (WD) connection. (a) 3W-CMC. (b) 4W-CMC. In these schematics TG stands for tracking generator, and SA stands for spectrum analyzer.

$$S_{21}^{\mathrm{WD}} = \frac{2RY_{\mathrm{D}}Y_{\mathrm{W}}}{Y_{\mathrm{D}} + Y_{\mathrm{W}} + 2RY_{\mathrm{D}}Y_{\mathrm{W}}} \tag{9b}$$

$$S_{21}^{\mathrm{OC}} = \frac{\dfrac{4RY_{\mathrm{C}}Y_{\mathrm{DN1}}Y_{\mathrm{DN2}}}{2Y_{\mathrm{C}}Y_{\mathrm{DN1}} + Y_{\mathrm{C}}Y_{\mathrm{DN2}} + Y_{\mathrm{DN1}}Y_{\mathrm{DN2}}}}{\dfrac{4RY_{\mathrm{C}}Y_{\mathrm{DN1}}Y_{\mathrm{DN2}}}{2Y_{\mathrm{C}}Y_{\mathrm{DN1}} + Y_{\mathrm{C}}Y_{\mathrm{DN2}} + Y_{\mathrm{DN1}}Y_{\mathrm{DN2}}} + 1} \tag{10a}$$

$$S_{21}^{\mathrm{WD-near}} = \frac{2RY_{\mathrm{DN1}}Y_{\mathrm{W}}}{Y_{\mathrm{DN1}} + Y_{\mathrm{W}} + 2RY_{\mathrm{DN1}}Y_{\mathrm{W}}} \tag{10b}$$

$$S_{21}^{\mathrm{WD-far}} = \frac{2RY_{\mathrm{DN2}}Y_{\mathrm{W}}}{Y_{\mathrm{DN2}} + Y_{\mathrm{W}} + 2RY_{\mathrm{DN2}}Y_{\mathrm{W}}}. \tag{10c}$$

Note that S_{21}^{OC} in (9a) and (10a) are proportional to all the resonant modal impedances of each CMC. Therefore, we expect to measure two resonances (related to Y_{C} and Y_{D} in Table III) in the insertion loss of the OC curve of a 3W-CMC, while a 4W-CMC should present three resonances related to the resonant admittances Y_{C}, Y_{DN1} and Y_{DN2} defined in (8). In the case of the WD connections, the response of the CMC should be proportional to the resonant differential admittances and to the admittance Y_{W}, which must be mainly capacitive. Considering that the main goal of WD measurement is to extract accurate information about Y_{W}, either $S_{21}^{\mathrm{WD-near}}$ or $S_{21}^{\mathrm{WD-far}}$ could be equally used to this end. In this work, we have used the measurement of $S_{21}^{\mathrm{WD-far}}$ for parameter extraction.

B. Step 2

Since we have assigned a physically meaningful basic circuit structure to the modal admittances of the CMC that appear in (9) and (10), the task of assigning values to these parameters for a particular CMC is therefore reduced to find the set of parameters that provides a better agreement between the measured curves of

TABLE VI
TYPICAL VALUES OF THE PSO ALGORITHM SETTING PARAMETERS

Parameter	Typical value
Maximum number of iterations	2000
Number of particles in the swarm	300
Particle velocity scaling factor	0.4
Scaling factor to search away from the particle's best known position	0.4
Scaling factor to search away from the swarm's best known position	0.8
Minimum change of swarm's best objective value before the search terminates	1e-9
Minimum change of swarm's best objective value before the search terminates	1e-9

the transmission coefficients in the OC and WD connections and the analytical expressions of these two transmission coefficients in (9) (for 3W-CMCs) or (10) (for 4W-CMCs). In this work, a particle swarm optimization (PSO) search algorithm has been used to this end [36]. This algorithm greatly benefits from the use of analytical expressions for the transmission coefficients and from the fact that the parameters of the MPC circuit model are independently associated with the different natural modes of the CMC. As a result, the typical computational time required to achieve a good fit ranges from a few seconds to a few minutes. To expedite the replicability of the results obtained with the method proposed in this work, we provide typical values for the setting parameters utilized in the PSO algorithm in Table VI.

It is worth mentioning that, to ensure a fast convergence of the search algorithm, it is convenient to provide suitable initial values for the parameters of the circuit model of the CMC. To this end, the self-inductance of a winding of the CMC can be measured with an *LCR*-meter, both in OC and in short-circuit configurations. This can be used along with the resonance frequencies, identified as sharp dips in the measured $|S_{21}^{\mathrm{OC}}|$ curves, to estimate the parasitic capacitances of the circuit model. Also, the magnitude of the transmission coefficient S_{21}^{OC} at the resonance frequencies can be used to estimate resistances in the *LCR* resonators. A detailed flowchart of the characterization technique outlined in this section can be seen in Fig. 6 within [19].

V. MODEL VERIFICATION

In general, assessing the feasibility and accuracy of a circuit model requires performing measurements to compare the actual response of the device with the prediction provided by the circuit model. In this work, we will check the accuracy of the models of 3W- and 4W-CMCs by using the standard tests defined in CISPR-17 to measure the interference suppression characteristics of passive filtering devices [37]. An schematic of these tests for characterizing 3W-CMCs is shown in Fig. 10. The test in Fig. 10(a) is referred to as asymmetrical mode test and it is intended to determine suppression of CM. The test in Fig. 10(b) is referred to as symmetrical mode test and allows measuring the response of the device to DMs.

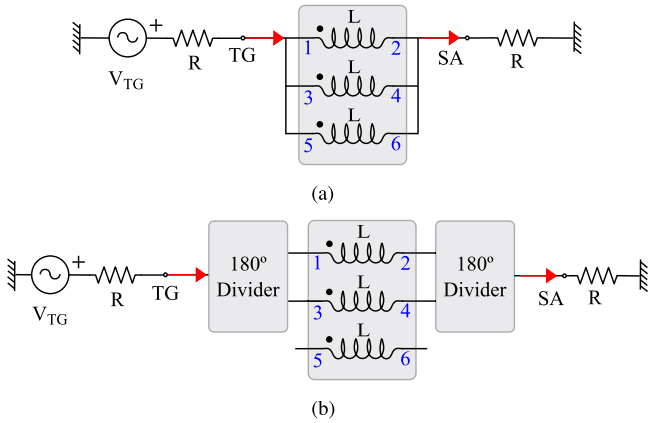

Fig. 10. CISPR-17 standard connections to characterize the insertion loss of a symmetric filtering device with six ports. (a) Asymmetrical mode or CM measurement setup. (b) Symmetrical mode or DM measurement setup.

By using the modal analysis presented in Section III, it is possible to obtain expressions for the transmission coefficients for asymmetrical and symmetrical mode tests in Fig. 10 (S_{21}^{asym} and S_{21}^{sym}) in terms of the modal admittances of the CMC. This provides a quick understanding about what these setups actually measure. For the case of the 3W-CMC, the following expressions are obtained:

$$S_{21}^{\mathrm{asym}} = \frac{2R(Y_{\mathrm{C}} - Y_{\mathrm{G}})}{(2RY_{\mathrm{C}} + 1)(2RY_{\mathrm{G}} + 1)} \tag{11}$$

$$S_{21}^{\mathrm{sym}} = \frac{2R(Y_{\mathrm{D}} - Y_{\mathrm{W}})}{(RY_{\mathrm{D}} + 2)(RY_{\mathrm{W}} + 2)}. \tag{12}$$

In these equations, it can be observed that the response of the 3W-CMC to the asymmetrical mode test is determined by Y_{C} and Y_{G}, whereas the response to symmetrical mode test is determined by Y_{D} and Y_{W}. These expressions are identical to those obtained for the 2W-CMC, [19].

Regarding the 4W-CMC, note that the transmission coefficient measured in the asymmetrical mode test setup is the same as that already provided for 3W-CMCs in (11). Thus, it can be deduced that, provided that proper care is taken in the measurements by putting the CMC sufficiently away from grounded surfaces, the asymmetrical mode test measures the response of the C mode of the 3W- or 4W-CMC, i.e., its attenuation of the CM in the three-wires or four-wires line. However, for a 4W-CMC with different mutual inductance coefficients for nearby and distant windings, two different expressions of the transmission coefficients for the symmetrical mode test can be obtained depending on whether the measurement involves two nearby coils or two distant coils

$$S_{21}^{\mathrm{sym-far}} = \frac{2R(Y_{\mathrm{DN2}} - Y_{\mathrm{W}})}{(RY_{\mathrm{DN2}} + 2)(RY_{\mathrm{W}} + 2)} \tag{13}$$

$$S_{21}^{\mathrm{sym-near}} = \frac{\dfrac{2RY_{\mathrm{DN1}}Y_{\mathrm{DN2}}}{Y_{\mathrm{DN1}} + Y_{\mathrm{DN2}}} - RY_{\mathrm{W}}}{\left(\dfrac{RY_{\mathrm{DN1}}Y_{\mathrm{DN2}}}{Y_{\mathrm{DN1}} + Y_{\mathrm{DN2}}} + 1\right)(RY_{\mathrm{W}} + 2)}. \tag{14}$$

TABLE VII
PARAMETERS OF THE MPC MODEL OF THE 3W- AND 4W-CMC CHARACTERIZED IN THIS PAPER

Manufacturer Part number	L* (mH)	C_C (pF)	CR in parallel with L_C			L_C (mH)	R_C (kΩ)	C_D (pF)	L_D	R_D	L_{D2} (μH)	R_{D2} (kΩ)	C_W (pF)	C_{sym} (pF)	LCR_W network		
			N_{CR}	C_1 (mH)	R_1 (kΩ)				L_{D1}** (μH)	R_{D1}** (kΩ)					L (μH)	C (pF)	R (kΩ)
EPCOS B82747S4423N020	1.5	5	1	19.3	12.7	4.9	14.7	3.8	5	4			28.4	-6.6	0.2	2.7	0.7
SCHAFFNER RD8147-25-1M3	1.3	36	1	28.2	11.5	5.1	61.8	37.1	4	3.6	8.9	3	57.6	45.4			

* Rated inductance. Information obtained from the data sheet.
** Corresponding to 4W-CMC.

Note that if $M_1 = M_2$ (and thus $Y_{DN1} = Y_{DN2}$), the expressions in (13) and (14) become equal to (12). For the more general case with $M_1 \neq M_2$, $S_{21}^{sym-far}$ in (13) has a structure similar to S_{21}^{sym} in (12), being the only difference the differential inductance involved ($L - M$ in the case of the 3W-CMC and $L - M_2$ in the case of the 4W-CMC). This means that this setup will measure the attenuation of the 4W-CMC to the components of the noise differentially exciting distant windings. It also means that we can expect a single resonance in this test when condition $Y_{DN2} - Y_W = 0$ is met. On the other hand, $S_{21}^{sym-near}$ in (14) has a more complicated structure that can be interpreted as the attenuation offered by the effect of Y_W along with the series combination of the Y_{DN1} and Y_{DN2} resonant admittances. For this reason, we can expect two resonances in this test.

From this analysis, it can be deduced that, since the symmetrical mode test performed on a pair of nearby windings excites the two natural differential admittances of a 4W-CMC, measuring both $S_{21}^{sym-near}$ and S_{21}^{asym} allows a thorough verification of the circuit model of the 4W-CMC.

VI. RESULTS

To evaluate the accuracy and scope of the characterization method proposed in this work, we have followed the procedure explained in the previous sections for obtaining and validating the MPC model of a large number of 3W-CMCs and 4W-CMCs. To perform the measurements, we used a R&S ZND vector network analyzer (VNA). For measurements with the symmetrical mode setup, we have used 180° dividers constructed with commercial wideband 1:1 transformers (Coilcraft WB2010-1). A comprehensive set of results for different commercial and custom-made 3W-CMCs and 4W-CMCs, with different core materials, is presented in a supplementary file [39]. In these results, we have concentrated in general on the 100 kHz–30 MHz frequency range because it coincides with that where many EMC standards (such as CISPR11 or CISPR22) impose limits on the conducted emissions of electronic equipment. However, the range has been extended for some CMCs that exhibit interesting behavior at lower or higher frequencies. In those cases, the lower limit of the CE102 section of the MIL-STD-461 standard (10 kHz) or the upper limit established in the aeronautical DO-160 standard for conducted emissions (153 MHz) has been chosen.

Results compiled in [39] demonstrate the accuracy and generality of the circuit model and characterization technique proposed in this work. The remainder of this section presents and discusses the results and the verification of the MPC model of two representative examples of CMCs for three phase systems: a 3W-CMCs and a 4W-CMCs. In addition, a final subsection presents results aimed at verifying the mode conversion effect that occurs in 4W-CMCs.

A. Results for a 3W-CMC

This section presents results of the characterization of a commercial 3W-CMC with a MnZn ferrite ring core. The part number of this 3W-CMC is listed in the first row of Table VII, along with the set of parameters obtained for its MPC model (see Fig. 4). It is worth noting that, for the case of 3W-CMCs, some of the authors of this article has previously developed a simpler circuit model and a characterization method based solely on the measurement of the S_{21}^{OC} transmission coefficient [25]. In this circuit model, which we will refer here to as simple-parameters circuit (SPC) model, the elements of the circuit are not associated with single modal admittances, which complicates determination of parameters values. Moreover, a major shortcoming of the SPC model is that the interwinding capacitors connect only nearby terminals, thus ignoring the dominant effect of the displacement currents through the high-permittivity core. Also, no WD measurement is performed in the characterization process. As a result, this method has some difficulties to accurately account for the high-frequency effects related to electric coupling between windings, yielding in general less precise results. Other second order effects accounted for by the MPC model, such as the impact of the change with frequency of the permeability of some materials or the possible presence of high-frequency resonances in the differential response of some 3W-CMCs, are not incorporated in the SPC model. Therefore, to highlight the improvements actually provided by the MPC model proposed in this work, we will systematically compare in this section the results of both models.

Fig. 11 shows, for the 3W-CMC analyzed in this section, the magnitude and phase of the S_{21}^{OC} transmission coefficient measured with the connection in Fig. 8. Note the presence of two resonances, in agreement with the prediction of the modal analysis (9a). Also, Fig. 12 shows graphs for the magnitude and phase of the S_{21}^{WD} measured as per the connection shown in Fig. 9 for this same 3W-CMC. Both Figs. 11 and 12 additionally include the S_{21}^{OC} and S_{21}^{WD} curves provided by the MCP and the SPC models once its parameters have been determined. The

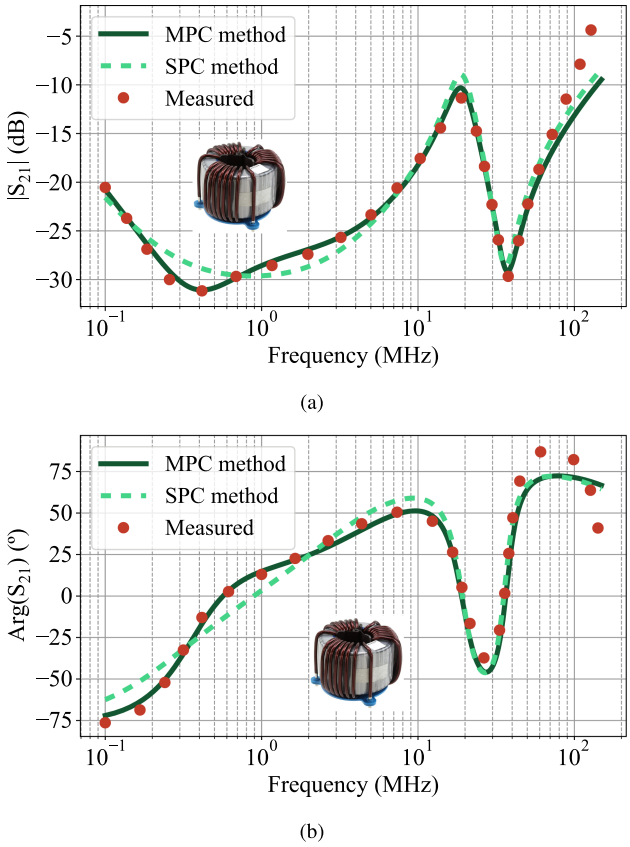

Fig. 11. Comparison of measured and calculated S_{21}^{OC} transmission coefficient for the 3W-CMC depicted in the inset (EPCOS B82747S4423N020). (a) Magnitude. (b) Phase. Parameters of the MPC and SPC models for this 3W-CMC are listed respectively in Tables VII and VIII.

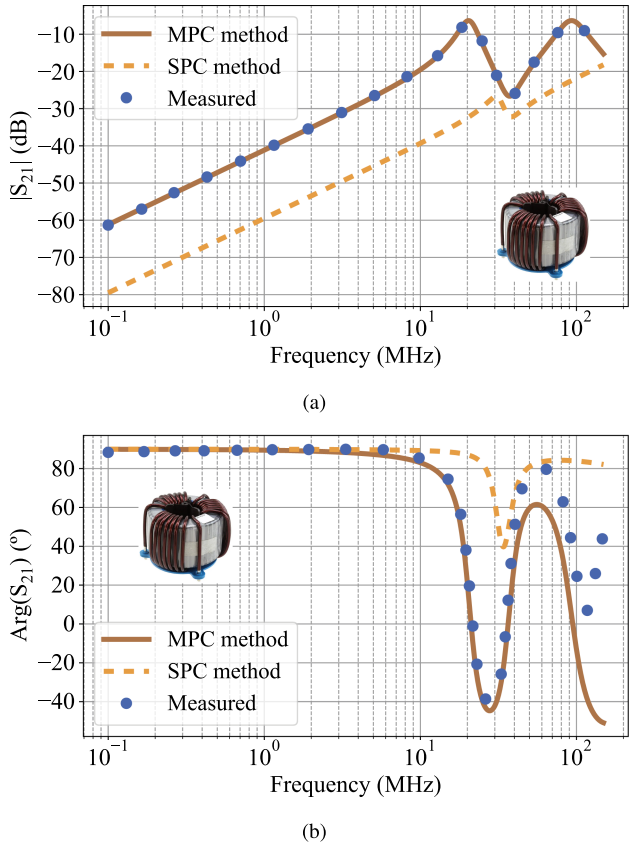

Fig. 12. Comparison of measured and calculated S_{21}^{WD} transmission coefficient for the 3W-CMC depicted in the inset (EPCOS B82747S4423N020). (a) Magnitude. (b) Phase. Parameters of the MPC and SPC models for this 3W-CMC are listed respectively in Tables VII and VIII.

TABLE VIII
PARAMETERS OF THE SPC MODEL (FIG. 1 IN [38]) FOR THE 3W-CMC CHARACTERIZED IN THIS PAPER

Manufacturer Part number	C_{t} (pF)	C_{W}[1] (pF)	$L+2M$ (mH)	R_1 (kΩ)	$L-M$ (μH)	R_2 (kΩ)
EPCOS B82747S4423N020	3.6	1.8	5.9	8.8	5.1	3.8

[1] C_{W} plays a different role in SPC than in MPC.

parameters of the MPC and SPC models are listed in Tables VII and VIII, respectively. A fair agreement can be observed between the measured S_{21}^{OC} curves and those of the MPC and SPC models, with the better results provided by the MPC model, which provides a very accurate approximation up to approximately 100 MHz. On the contrary, the results for S_{21}^{WD} in Fig. 14 show that while the MPC model accurately accounts for the response of the CMC in this connection, the SPC method is unable to approximate the S_{21}^{WD} curves. As explained above, this is related to the fact that the characterization process proposed in [25] only makes use of $|S_{21}^{\mathrm{OC}}|$. This, along with the unsuitability of the SPC model to accurately account for the effect of the interwinding electric couplings in practical 3W-CMCs, undermines accuracy of the SPC model.

It is also worth noting that, as shown in Figs. 11(b) and 12(b), the MPC model accurately accounts for the phases of S_{21}^{OC} and S_{21}^{WD}, despite the fact that only the magnitudes of these transmission coefficients are used to find the parameters of the MPC model. This is a general result for all the analyzed CMCs, and it can be understood by realizing that the MPC model is a physically based model, as opposed to a purely behavioral model. Also, in the parameters listed in Table VII for this 3W-CMC it can be seen that in this case the MPC model includes an additional *RC* branch within its asymmetrical test block, which corresponds to the Y_{RLC} impedance in Fig. 4. This inclusion significantly enhances the accuracy of S_{21}^{OC} by taking into account the effect of dielectric losses in the core [19]. The MPC model of this 3W-CMC also integrates a LCR_{W} network within Y_{W}, which accounts for inter-turn resonances [19].

As explained in Section III, a convenient approach to validate the circuit model of a CMC is to compare the prediction of the model with the measured responses of the CMC in both the asymmetrical mode and symmetrical mode tests established in CISPR-17 norm [37]. This has been done for both the MPC model and the SPC model of this 3W-CMC, and results are displayed in Figs. 13 and 14. Note that the MPC model provides a very good prediction of the response of the CMC, and that its accuracy is higher than that of the SPC model. This is

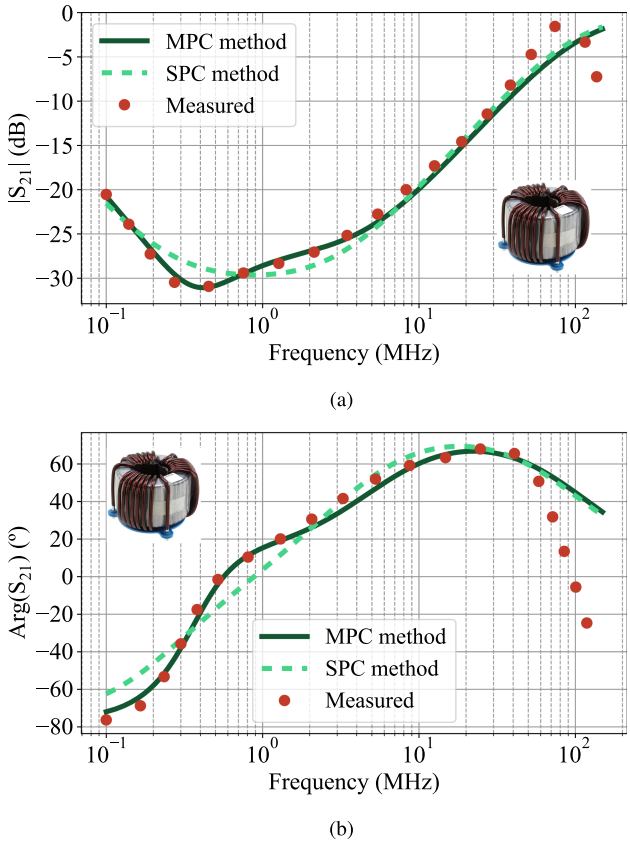

Fig. 13. Comparison of measured and calculated transmission coefficient in CISPR-17 asymmetrical mode test (S_{21}^{asym}) for the 3W-CMC depicted in the inset (EPCOS B82747S4423N020). (a) Magnitude. (b) Phase. Parameters of the MPC and SPC models for this 3W-CMC are listed in Tables VII and VIII, respectively.

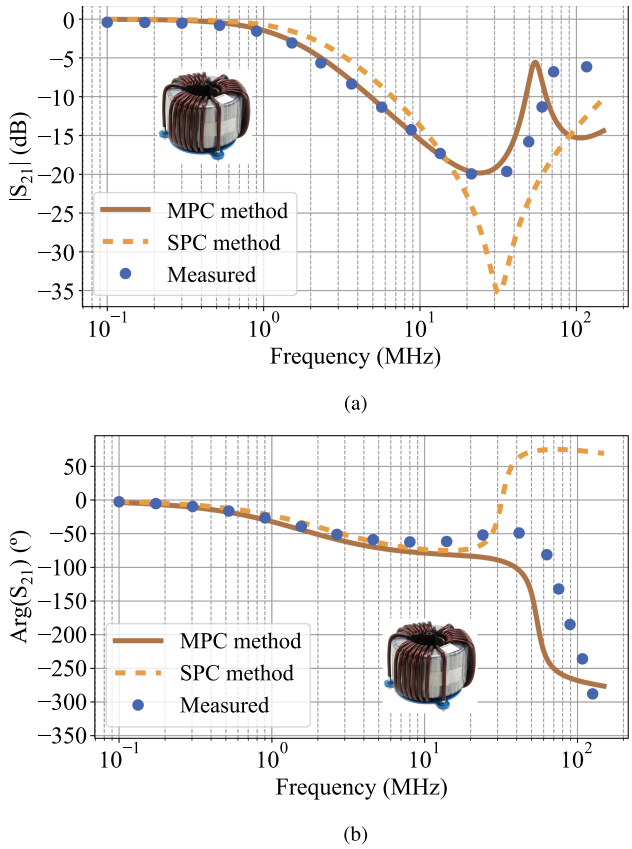

Fig. 14. Comparison of measured and calculated transmission coefficient in CISPR-17 symmetrical mode test (S_{21}^{sym}) for the 3W-CMC depicted in the inset (EPCOS B82747S4423N020). (a) Magnitude. (b) Phase. Parameters of the MPC and SPC models for this 3W-CMC are listed in Tables VII and VIII, respectively.

particularly noticeable for the symmetrical mode test, mainly due to improved accuracy in the definition and determination of Y_{W}, as explained in [19]. In general, the MPC model demonstrates a high level of accuracy up to frequencies of several tens of MHz. Beyond these frequencies, this 3W-CMC exhibits higher-order resonances, likely attributed to transmission line effects resulting from a short wavelength inside the core. These resonances are not accounted for by the MPC model. While it is possible to address these effects by introducing additional resonant tanks in the MPC model, the resultant increase in model complexity may not be justified in most cases for two primary reasons. First, these effects typically manifest at frequencies exceeding the upper frequency where the limits to conducted emissions are established by the EMC regulations. Second, at those high frequencies, the attenuation actually provided by the CMC uses to be already quite poor. Consequently, the impact of the CMC on the overall performance of an EMI filter is expected to be negligible when compared with other high-frequency effects [40], [41].

B. Results for a 4W-CMC

In this section, we will obtain and verify the MPC model of a commercial 4W-CMC, listed in the second row of Table VII. Fig. 15 shows the magnitude of the S_{21}^{OC} and S_{21}^{WD} transmission coefficients of this 4W-CMC, corresponding to the setups described in Figs. 8(b) and 9(b). These results demonstrate that the MPC model is able to accurately reproduce $|S_{21}^{\text{OC}}|$ and $|S_{21}^{\text{WD}}|$ for this 4W-CMC. A similar accuracy is obtained in the phase of these transmission coefficients (not shown). It is interesting to note that the curve of $|S_{21}^{\text{OC}}|$ of this 4W-CMC exhibits three resonances (dips). This is in contrast to the two resonances that can typically be observed in the S_{21}^{OC} curves of 2W- or 3W-CMCs. As explained in Section IV, this can be accounted for by the difference existing between the mutual inductances of nearby and distant windings in 4W-CMCs with windings evenly distributed on the core.

The precision of the MPC model is further verified by the good agreement shown in Fig. 16 between measured and calculated transmission coefficients of this 4W-CMC in both the asymmetrical and the symmetrical mode test setups. Regarding the response to symmetrical mode test, it is worth mentioning that because it corresponds to an excitation of adjacent windings, two distinct resonances can be observed in the S_{21}^{sym} curve, as expected from the analysis in Section V.

C. Mode Conversion in a 4W-CMC

The analysis carried out in Section III-B1 predicts that the 4W-CMC will provoke conversion between modes H, D1 and

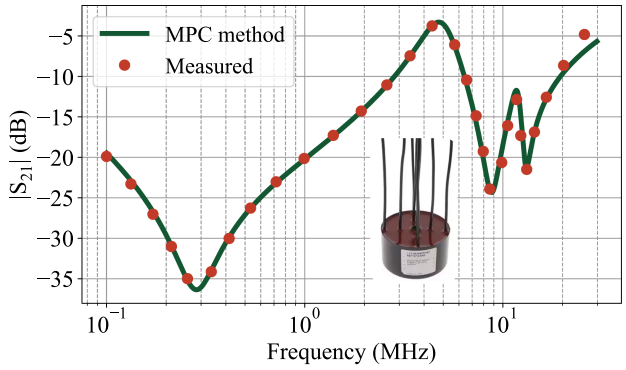

(a)

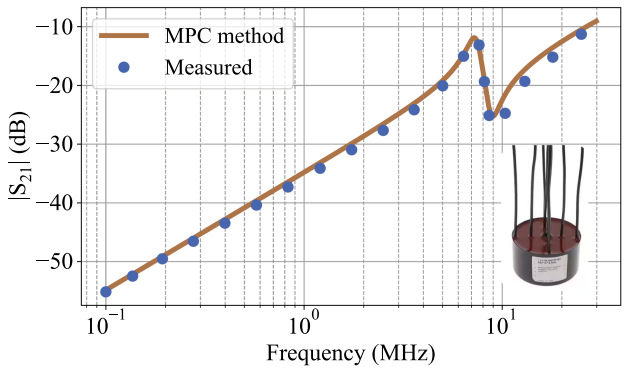

(b)

Fig. 15. Comparison of measured and calculated S_{21}^{OC} and S_{21}^{WD} transmission coefficients for the 4W-CMC depicted in the inset (SCHAFFNER RD8147-25-1M3). Parameters of the MPC model for this 4W-CMC are listed in Table VII.

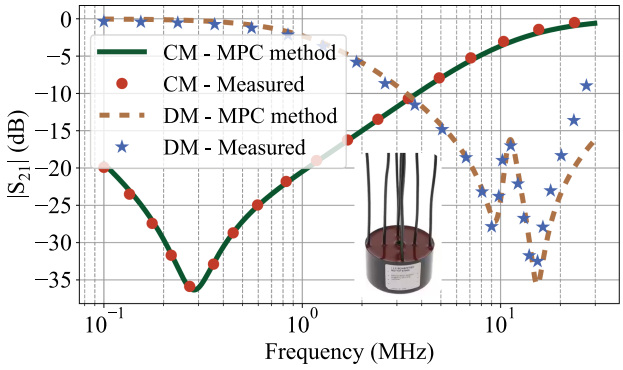

Fig. 16. Comparison of measured and calculated S_{21}^{asym} and S_{21}^{sym} transmission coefficients for the 4W-CMC depicted in the inset (SCHAFFNER RD8147-25-1M3). The parameters of the MPC model for this 4W-CMC are listed in Table VII.

D2 due to a difference between the mutual inductances of nearby and distant windings. As a consequence, the presence of the 4W-CMC on a four-wires ($N = 4$) line will cause conversion between DM currents (DM1 and DM2 modes in Table I) and noise currents propagating in homopolar mode (CM2 mode in Table I).

A convenient way to quantify mode conversion in any device is to calculate its mixed-mode S-parameter matrix. The mixed-mode S-parameter matrix was defined to characterize CM and DM propagation and conversion in differential lines [42], [43]. However, this concept can be easily generalized to deal with mode propagation and conversion in a general N-conductors line [20]. In essence, the idea is to calculate the singled-ended S-parameter matrix and then perform a change of basis, as shown in Appendix A [see equations (24) to (26)]. In the particular case of the four-wires line, a device inserted in the line has 8 ports. Then, by assigning numbers 1 to 4 to input ports and 5 to 8 to output ports, the 8×8 change-of-basis matrix can be expressed in the following form:

$$\boldsymbol{M_{4W}} = \begin{bmatrix} \boldsymbol{T_{4W}} & \mathbf{0} \\ \mathbf{0} & \boldsymbol{T_{4W}} \end{bmatrix}. \tag{15}$$

Here, $\boldsymbol{T_{4W}}$ defines the four modes in the line, which in our case are given in (1). This should give rise to a 8×8 mixed mode S parameters matrix with the following form:

$$\boldsymbol{S_{mm}} = \begin{bmatrix} \boldsymbol{S_{11}} & \boldsymbol{S_{12}} \\ \boldsymbol{S_{21}} & \boldsymbol{S_{22}} \end{bmatrix} \tag{16}$$

where $\boldsymbol{S_{ij}}$ with $i, j = 1, 2$ are 4×4 matrices that represent the reflection coefficients at the input ($\boldsymbol{S_{11}}$) and output ($\boldsymbol{S_{22}}$) ports of the device or the transmission coefficients of the modes ($\boldsymbol{S_{21}} = \boldsymbol{S_{12}}^t$). In our case, $\boldsymbol{S_{21}}$ is a symmetric matrix that can be written as

$$\boldsymbol{S_{21}} = \begin{bmatrix} S_{21}^{C-C} & S_{21}^{C-H} & S_{21}^{C-D1} & S_{21}^{C-D2} \\ S_{21}^{C-H} & S_{21}^{H-H} & S_{21}^{H-D1} & S_{21}^{H-D2} \\ S_{21}^{C-D1} & S_{21}^{H-D1} & S_{21}^{D1-D1} & S_{21}^{D1-D2} \\ S_{21}^{C-D2} & S_{21}^{H-D2} & S_{21}^{D1-D2} & S_{21}^{D2-D2} \end{bmatrix} \tag{17}$$

where the four elements in the diagonal are the transmission coefficients of each mode of the line. For example, S_{21}^{C-C} is the transmission coefficient of the C mode, which quantifies the effect of the 4W-CMC on the CM1 mode of the line, while S_{21}^{H-H} quantifies the transmission of the CM2 or homopolar mode of the line. On the other hand, elements off the diagonal of $\boldsymbol{S_{21}}$ in (17) represent mode conversion between each pair of modes of the line. In our case, the MPC model of the 4W-CMC proposed in this work (see Fig. 7) accounts for the effect of mode conversion between mode H and modes D1 and D2, but no mode conversion is expected between mode C and the other modes, as explained in Section III-B1. As a consequence, when the mixed-mode S-parameter matrix is calculated for the MPC circuit model of the 4W-CMC, we get $S_{21}^{C-H} = S_{21}^{C-D1} = S_{21}^{C-D2} = 0$, whereas a mode conversion between H, D1 y D2 modes is predicted and given by the following analytical expressions for the corresponding mixed-mode S parameters:

$$S_{21}^{H-D1} = \frac{-K}{3\sqrt{2}} \tag{18a}$$

$$S_{21}^{H-D2} = \frac{K}{\sqrt{6}} \tag{18b}$$

Fig. 17. 4W-CMC (SCHAFFNER RD8147-25-1M3) mounted on a PCB for measuring single-ended S-parameters with a two-ports VNA.

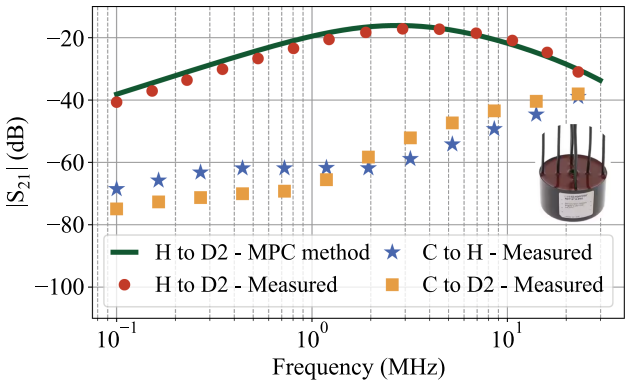

Fig. 18. Measured mixed-mode S-parameters quantifying conversion between modes for the 4W-CMC of SCHAFFNER whose details are provided in Table VII. The predicted conversion between the H and D2 noise modes calculated using the MPC model of 4W-CMC is also represented.

$$S_{21}^{D1-D2} = \frac{-K}{2\sqrt{3}} \tag{18c}$$

where

$$K = \frac{R_0\left(Y_{\mathrm{DN1}} - Y_{\mathrm{DN2}}\right)}{\left(1 + R_0 Y_{\mathrm{DN1}}\right)\left(1 + R_0 Y_{\mathrm{DN2}}\right)}. \tag{19}$$

Note that these mode-conversion transmission coefficients are proportional to K in (19), and hence to the difference $Y_{\mathrm{DN1}} - Y_{\mathrm{DN2}}$, which implies that they increase with the difference between M_1 and M_2 mutual inductances and also that no mode conversion should be expected in the case $M_1 = M_2$.

To verify this prediction, we have measured the 8×8 single-ended S parameters of the 4W-CMC SCHAFFNER RD8147-25-1M3 in Table VII. Then, we have performed a change of basis to obtain the mixed-mode S-parameter matrix of this 4W-CMC and we have compared the coefficients of this matrix with those analytically obtained for the MPC model of this 4W-CMC with the parameters given in in Table VII. To measure the elements of the S-parameter matrix, the 4W-CMC is mounted in a FR4 1.5 mm-thick printed circuit board with 3 mm-width traces and a return plane, which is shown in Fig. 17. Measurements have been carried out with a two-port VNA, matching all ports with a 50 Ω load [20], [43].

Fig. 18 shows measured S_{21}^{H-D2}, S_{21}^{C-H} and S_{21}^{C-D2} elements of the mixed-mode S-parameters matrix of this 4W-CMC. As expected, S_{21}^{C-H} and S_{21}^{C-D2} have quite small values in all the frequency range, which indicates that only residual mode conversion is caused by the 4W-CMC between mode C and modes H and D2. Interestingly, these mode conversions increase with frequency, which reveals the effect of small construction asymmetries of the device and/or of the measuring setup [20]. Also expectedly, it can be observed in Fig. 18 that S_{21}^{H-D2} takes nonnegligible values in the entire 100 kHz–30 MHz frequency range represented in that graph. As already explained, this is caused by the fact that the mutual coupling coefficients of the windings are different for nearby and distant coils. To demonstrate this, the calculated S_{21}^{H-D2} for the MPC model of this 4W-CMC has also been represented in Fig. 18. Note that the calculated and measured S_{21}^{H-D2} curves agree very well. Similar results are obtained for S_{21}^{H-D1} and S_{21}^{D1-D2} (not shown). This demonstrates the accuracy of the MPC model and also highlights the power of the modal analysis, which enables obtaining analytical expressions for mixed-mode S parameters in terms of the modal admittances of the CMC (18), thus making it possible to quantify the mode conversion caused by the CMC in a straightforward manner.

VII. Conclusion

In this work, an efficient method has been presented to obtain a highly accurate and wideband equivalent circuit model for 3-wire and 4-wire CMC used for filtering noise in the power lines of three-phase systems. A detailed analysis, aimed at understanding and quantifying the effect of these CMCs on the transmission modes in three-phase lines, has been provided. This work constitutes a nontrivial extension of a previous study focused on 2-wire CMCs for single-phase systems. Specifically, an extension of the idea of modal analysis for these types of devices has been carried out. A key contribution of this work is to establish the relationship that must exist between the noise propagation modes defined in the three-phase line and the natural modes of a CMC (as a six- or eight-port device) to ensure that the CMC does not cause mode conversion in the line. A prior definition of modes in three-phase lines was necessary to carry out this analysis.

The key idea of this work is that it should be possible to accurately predict the response of a 3W-CMC or a 4W-CMC in any connection once the device's response to each of its natural modes has been properly characterized. Based on this idea, an equivalent circuit model called MPC model is proposed for both 3W-CMC and 4W-CMCs, fulfilling two fundamental requirements aimed at optimizing the accuracy of the circuit models and at facilitating the identification of the values of the circuits parameters. First, its elements are grouped into independent blocks, each associated only with one of the natural modes of the CMC. Second, each block is associated with a basic circuit model according to what is expected from the physical phenomenon it represents.

The modal analysis presented in this work has allowed us to demonstrate that it is possible to use a pair of simple

measurement setups that reveal the CMC's response to all its modal excitations. Interestingly, these setups are quite similar to those proposed in [19] for 2W-CMCs, which makes this demonstration a remarkable and nonobvious result. A characterization technique based on advanced search algorithms has been designed, benefiting from the particular convenience of both the proposed circuit models and the measurement setups, to efficiently and accurately determine all parameters of the 3W- and 4W-CMC circuit models. The proposed circuit model and characterization method have been thoroughly checked by characterizing a large number of 3W- and 4W-CMCs. It has been verified that, for the connections proposed by the CISPR17 standard to characterize passive filtering components, the MPC model provides a quite accurate prediction of the measured response of these CMCs within a sufficiently wide frequency range.

Another noteworthy result is that, for the case of 4W-CMCs in their most common presentation (i.e., four coils symmetrically distributed in the core), it is demonstrated that mode conversion between homopolar and DMs in the three-phase line should be expected. Moreover, the proposed circuit model and characterization technique allow predicting and quantifying this mode conversion. Since the modal analysis presented here allows for a systematic, efficient and detailed study of additional mode conversions caused by the asymmetric construction of CMCs, this is proposed as an interesting future work.

Appendix A
Reciprocal $2N$-Ports Network With no Mode Conversion

In this appendix, we analyze the necessary and sufficient condition to avoid mode conversion in a $2N$-port device with N input ports and N output ports and input/output symmetry, when inserted in a transmission line of $N+1$ conductors (N modes). This general situation is schematized in Fig. 19. By input/output symmetry, we mean that the N input ports are interchangeable with the N output ports with no change in the input and output voltages and currents. This condition is met in general by CMCs. In this appendix, we will use the numeration of ports shown in Fig. 19, with the first N ports indicating input ports and the last N ports referring to output ports. As we will see, this arrangement of the number of the ports allows simplifying notation and calculations for this general $2N$-ports case.

Let $\boldsymbol{T}$ be a orthonormal $N \times N$ matrix whose columns define N linearly independent transmission modes in the $N+1$-conductors transmission line where the $2N$-ports device is connected. It can be demonstrated that a necessary and sufficient condition to ensure that a reciprocal $2N$-ports network with input/output symmetry (such as a CMC) causes no energy transfer between modes is that the eigenvectors of the admittance matrix of the device are given by the columns of the following $2N \times 2N$ matrix:

$$\boldsymbol{E} = \begin{bmatrix} \boldsymbol{T} & \boldsymbol{T} \\ \boldsymbol{T} & -\boldsymbol{T} \end{bmatrix} = \begin{bmatrix} 1 & 1 \\ 1 & -1 \end{bmatrix} \otimes \boldsymbol{T} \tag{20}$$

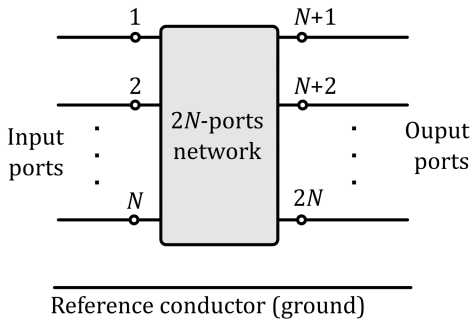

Fig. 19. $2N$-ports device connected in a $N+1$-conductors transmission line.

where we have made use of the Kronecker product to simplify the notation and facilitate the subsequent calculations [44].

To demonstrate this, let first analyze the restrictions imposed by the symmetry of the device and the mathematical condition that ensures no mode conversion.

With respect to the first point. In general, any filtering device inserted in a $N+1$ conductors transmission line can be considered as a $2N$-ports device, which can be modeled by a $2N$-ports reciprocal network characterized by a $2N \times 2N$ admittance matrix, $\boldsymbol{Y}$. In case the filtering device has input/output symmetry, it can be easily demonstrated that $\boldsymbol{Y}$ expressed in the terminal's basis must have the following form:

$$\boldsymbol{Y} = \begin{bmatrix} \boldsymbol{Y_i} & \boldsymbol{Y_j} \\ \boldsymbol{Y_j} & \boldsymbol{Y_i} \end{bmatrix} \tag{21}$$

where $\boldsymbol{Y_i}$ and $\boldsymbol{Y_j}$ are symmetric $N \times N$ matrices.The admittance matrix $\boldsymbol{Y}$ in (21) can be rewritten in a convenient way by using the Kronecker product [44]

$$\boldsymbol{Y} = \begin{bmatrix} 1 & 0 \\ 0 & 1 \end{bmatrix} \otimes \boldsymbol{Y_i} + \begin{bmatrix} 0 & 1 \\ 1 & 0 \end{bmatrix} \otimes \boldsymbol{Y_j}. \tag{22}$$

A convenient way to determine whether this device causes mode conversion between that particular set of modes is to calculate the mixed-mode S-parameters matrix of the device. To this end, the $2N \times 2N$ S-matrix of the $2N$-ports network can be calculated as [45]

$$\boldsymbol{S} = (\boldsymbol{I} + \boldsymbol{Y_n})^{-1} \cdot (\boldsymbol{I} - \boldsymbol{Y_n}) \tag{23}$$

where $\boldsymbol{I}$ stands for the $2N \times 2N$ identity matrix and $\boldsymbol{Y_n}$ is the admittance matrix of the $2N$-ports network normalized with respect to the input and output impedances (usually $R = 50\ \Omega$). From $\boldsymbol{S}$ in (23), the mixed-mode S-parameter matrix of the $2N$-ports network can be calculated by performing a change of basis

$$\boldsymbol{S_{mm}} = \boldsymbol{M}^{-1} \cdot \boldsymbol{S} \cdot \boldsymbol{M} \tag{24}$$

where $\boldsymbol{M}$ is the change-of-basis matrix from the mixed-mode basis to the standard basis of the terminals

$$\boldsymbol{M} = \begin{bmatrix} 1 & 0 \\ 0 & 1 \end{bmatrix} \otimes \boldsymbol{T}. \tag{25}$$

The mixed-mode S-parameter matrix of a reciprocal device with input/output symmetry can in general be expressed as follows:

$$\boldsymbol{S_{mm}} = \begin{bmatrix} 1 & 0 \\ 0 & 1 \end{bmatrix} \otimes \boldsymbol{S_i} + \begin{bmatrix} 0 & 1 \\ 1 & 0 \end{bmatrix} \otimes \boldsymbol{S_j} \tag{26}$$

where the terms in $\boldsymbol{S_i}$ are the reflection coefficients of the N modes of the line and the terms in $\boldsymbol{S_j}$ are the transmission coefficients. Thus, *the key condition that ensures no mode conversion in the line is that both $\boldsymbol{S_i}$ and $\boldsymbol{S_j}$ are purely diagonal matrices.*

Let therefore first assume that the columns of $\boldsymbol{E}$ in (20) are eigenvalues of the admittance matrix of the $2N$-network and let demonstrate that this is a sufficient condition to ensure no mode conversion between the modes defined by $\boldsymbol{T}$ in the transmission line. Since $\boldsymbol{E}$ is actually a change of basis matrix from the basis of the eigenvalues to the terminals basis, this can be used to calculate the admittance matrix in the basis of its eigenvectors as: $\boldsymbol{Y_e} = \boldsymbol{E}^{-1} \cdot \boldsymbol{Y} \cdot \boldsymbol{E}$. Since the vectors in $\boldsymbol{E}$ are eigenvectors of $\boldsymbol{Y}$, this means that the admittance matrix $\boldsymbol{Y_e}$ must be diagonal, being the terms of the diagonal the modal admittances (or eigenvalues). The mixed-mode S-parameter matrix of the device can then be calculated by firstly calculating the S-parameter matrix in the modal basis, $\boldsymbol{S_e}$, from $\boldsymbol{Y_e}$ using (23) and then carrying out a change of basis form the basis of the eigenvectors to the mixed-mode basis

$$\boldsymbol{S_{mm}} = \boldsymbol{M}^{-1} \cdot \boldsymbol{E} \cdot \boldsymbol{S_e} \cdot \boldsymbol{E}^{-1} \cdot \boldsymbol{M} \tag{27}$$

where

$$\boldsymbol{M}^{-1} \cdot \boldsymbol{E} = \begin{bmatrix} 1 & 1 \\ 1 & -1 \end{bmatrix} \otimes \boldsymbol{I} \tag{28}$$

$$\boldsymbol{E}^{-1} \cdot \boldsymbol{M} = (\boldsymbol{M}^{-1} \cdot \boldsymbol{E})^{-1} = \frac{1}{2} \begin{bmatrix} 1 & 1 \\ 1 & -1 \end{bmatrix} \otimes \boldsymbol{I}. \tag{29}$$

By assuming that $\boldsymbol{S_e}$ is diagonal, and making use of the basic rules of the algebra of the Kronecker product [44], it can be demonstrated that $\boldsymbol{S_{mm}}$ has the form described in (26), where $\boldsymbol{S_i}$ and $\boldsymbol{S_j}$ are diagonal matrices. This allows us to conclude that this $2N$-ports network does not cause conversion between the modes defined in the line.

It is also possible to demonstrate that the fact that the columns of $\boldsymbol{E}$ in (20) are eigenvalues of the admittance matrix of the $2N$-network is a necessary condition to ensure that no mode conversion exists in the transmission line. To do that, let us assume that the mixed-mode S-parameter matrix of the $2N$-ports network $\boldsymbol{S_{mm}}$, defined for the line modes given by $\boldsymbol{T}$, has the form shown in (26), with purely diagonal $\boldsymbol{Si}$ and $\boldsymbol{Sj}$ matrices. This is equivalent to assuming that this device will not cause mode conversion. From $\boldsymbol{S_{mm}}$, it is possible to calculate the S-matrix in the base defined by $\boldsymbol{E}$

$$\boldsymbol{S_e} = \boldsymbol{E}^{-1} \cdot \boldsymbol{M} \cdot \boldsymbol{S_{mm}} \cdot \boldsymbol{M}^{-1} \cdot \boldsymbol{E} \tag{30}$$

where the change of basis matrix and its inverse are given by (28) and (29). By performing this calculation, it can be verified that $\boldsymbol{S_e}$ is a diagonal matrix with the following form:

$$\boldsymbol{S_e} = \begin{bmatrix} 1 & 0 \\ 0 & 1 \end{bmatrix} \otimes \boldsymbol{S_i} + \begin{bmatrix} 1 & 0 \\ 0 & -1 \end{bmatrix} \otimes \boldsymbol{S_j}. \tag{31}$$

Then, the admittance matrix expressed in the same basis $\boldsymbol{E}$ can be obtained as [45]

$$\boldsymbol{Y_e} = (\boldsymbol{I} - \boldsymbol{S_e}) \cdot (\boldsymbol{I} + \boldsymbol{S_e})^{-1}. \tag{32}$$

Since $\boldsymbol{Y_e}$ is obtained as the product of two diagonal matrices, $\boldsymbol{Y_e}$ must be diagonal, which indicates that the column vectors of $\boldsymbol{E}$ are eigenvectors of the admittance matrix of the $2N$-ports network.

REFERENCES

[1] B. Zhang and S. Wang, "A survey of EMI research in power electronics systems with wide-bandgap semiconductor devices," *IEEE Trans. Emerg. Sel. Topics Power Electron.*, vol. 8, no. 1, pp. 626–643, Mar. 2020.

[2] *Industrial, Scientific, and Medical Equipment-Radio-Frequency Disturbance Characteristics: Limits and Methods of Measurement*, IEC CISPR Standard EN55011:2011/CISPR 11, 2010.

[3] *Environmental Conditions and Test Procedures for Airborne Equipment*, RTCA/DO-160G - Section 21 - Emission of Radio Frequency Energy, RTCA, Inc., Dec. 8, 2010.

[4] MIL-STD-461G, "Requirements for the control of electromagnetic interference characteristics of subsystems and equipment," Dept. Defense, USA, 2015.

[5] C. R. Paul, *Introduction to Electromagnetic Compatibility*. Hoboken, NJ, USA: Wiley, 2006.

[6] M. Nave, *Power Line Filter Design for Switched-Mode Power Supplies*. New York, NY, USA: Van Nostrand Reinhold, 1991.

[7] R. Zhang, V. H. Prasad, D. Boroyevich, and F. C. Lee, "Three-dimensional space vector modulation for four-leg voltage-source converters," *IEEE Trans Power Electron*, vol. 17, no. 3, pp. 314–326, May 2002.

[8] Z. Zhao, B. Horn, and R. Leidhold, "Optimized filter design for common-mode current reduction in four-wire inverter-fed motors," *IEEE Trans. Ind. Electron.*, vol. 69, no. 3, pp. 2265–2275, Mar. 2022.

[9] Z. Liu, J. Liu, and J. Li, "Modeling, analysis, and mitigation of load neutral point voltage for three-phase four-leg inverter," *IEEE Trans. Ind. Electron.*, vol. 60, no. 5, pp. 2010–2021, May 2013.

[10] A. Roc'h, H. Bergsma, D. Zhao, B. Ferreira, and F. Leferink, "A new behavioural model for performance evaluation of common mode chokes," in *Proc. 18th Int. Zurich Symp. Electromagn. Compat.*, 2007, pp. 501–504.

[11] J. L. Kotny, X. Margueron, and N. Idir, "High-frequency model of the coupled inductors used in EMI filters," *IEEE Trans. Power Electron.*, vol. 27, no. 6, pp. 2805–2812, Jun. 2012.

[12] I. Stevanovic, S. Skibin, M. Masti, and M. Laitinen, "Behavioral modeling of chokes for EMI simulations in power electronics," *IEEE Trans. Power Electron.*, vol. 28, no. 2, pp. 695–705, Feb. 2013.

[13] W. Tan, C. Cuellar, X. Margueron, and N. Idir, "A high frequency equivalent circuit and parameter extraction procedure for common mode choke in the EMI filter," *IEEE Trans. Power Electron.*, vol. 28, no. 3, pp. 1157–1166, Mar. 2013.

[14] M. Kovacic, Z. Hanic, S. Stipetic, S. Krishnamurthy, and D. Zarko, "Analytical wideband model of a common-mode choke," *IEEE Trans. Power Electron.*, vol. 27, no. 7, pp. 3173–3185, Jul. 2012.

[15] I. F. Kovacevic, T. Friedli, A. M. Musing, and J. W. Kolar, "3-D electromagnetic modeling of parasitics and mutual coupling in EMI filters," *IEEE Trans. Power Electron.*, vol. 29, no. 1, pp. 135–149, Jan. 2014.

[16] I. F. Kovacevic, T. Friedli, A. M. Muesing, and J. W. Kolar, "3-D electromagnetic modeling of EMI input filters," *IEEE Trans. Ind. Electron.*, vol. 61, no. 1, pp. 231–242, Jan. 2014.

[17] C. Dominguez-Palacios, J. Bernal-Méndez, and M. A. Martín-Prats, "Characterization of common mode chokes at high frequencies with simple measurements," *IEEE Trans. Power Electron.*, vol. 33, no. 5, pp. 3975–3987, May 2018.

[18] F. Salomez, A. Videt, and N. Idir, "Modeling and minimization of the parasitic capacitances of single-layer toroidal inductors," *IEEE Trans. Power Electron.*, vol. 37, no. 10, pp. 12426–12436, Oct. 2022.

[19] A. Ojeda-Rodríguez, J. Bernal-Méndez, and M. Martín-Prats, "Modal theory and approach for accurate characterization of common-mode chokes," *IEEE Trans. Power Electron.*, vol. 38, no. 9, pp. 10516–10529, Sep. 2023.

[20] J. Wei, D. Gerling, and M. Galek, "S-parameters characterization and sequence model of three-phase EMI filter," in *Proc. IECON Proc. (Ind. Electron. Conf.)*, 2013, pp. 1254–1259.

[21] D. Han, C. T. Morris, W. Lee, and B. Sarlioglu, "Three-phase common mode inductor design and size minimization," in *Proc. IEEE Transp. Electrif. Conf. Expo.*, 2016, pp. 1–8.

[22] S. Li, S. Lu, and C. C. Mi, "Revolution of electric vehicle charging technologies accelerated by wide bandgap devices," *Proc. IEEE*, vol. 109, no. 6, pp. 985–1003, Jun. 2021.

[23] S.-P. Weber, E. Hoene, S. Guttowski, J. John, and H. Reichl, "Predicting parasitics and inductive coupling in emi-filters," in *Proc. IEEE 21st Annu. Appl. Power Electron. Conf. Expo.*, 2006, pp. 1157–1160.

[24] M. L. Heldwein, L. Dalessandro, and J. W. Kolar, "The three-phase common-mode inductor: Modeling and design issues," *IEEE Trans. Ind. Electron.*, vol. 58, no. 8, pp. 3264–3274, Aug. 2011.

[25] C. Dominguez-Palacios, J. Bernal-Méndez, and M. A. M. Prats, "Characterization of three-phase common-mode chokes at high frequencies," *IEEE Trans. Power Electron.*, vol. 33, no. 8, pp. 6471–6475, Aug. 2018.

[26] C. R. Paul, *Analysis of Multiconductor Transmission Lines*, 2nd ed. Hoboken, NJ, USA: Wiley, 2008.

[27] F. D. Torre, S. Leva, and A. P. Morando, "A physical decomposition of three-phase variables into common and differential mode quantities," in *Proc. IEEE 18th Int. Zurich Symp. Electromagn. Compat.*, 2007, pp. 127–130.

[28] D. Drozhzhin, "Consideration of electromagnetic noise during design of inverter for transportation applications," Ph.D. dissertation, Technische Univ. Darmstadt, Darmstadt, Germany, 2020.

[29] H. Hizarci, U. Pekperlak, and U. Arifoglu, "Conducted emission suppression using an EMI filter for grid-tied three-phase/level T-type solar inverter," *IEEE Access*, vol. 9, pp. 67417–67431, 2021.

[30] P. Papamanolis, D. Bortis, F. Krismer, D. Menzi, and J. W. Kolar, "New EV battery charger PFC rectifier front-end allowing full power delivery in 3-Phase and 1-Phase operation," *Electron. (Switzerland)*, vol. 10, no. 17, pp. 1–33, 2021.

[31] E. Clarke, "Problems solved by modified symmetrical components," *Gen. Electric Rev.*, vol. 41, no. 11–12, pp. 488–494, 1938.

[32] C. J. O'Rourke, M. M. Qasim, M. R. Overlin, and J. L. Kirtley, "A geometric interpretation of reference frames and transformations: Dq0, clarke, and park," *IEEE Trans. Energy Convers.*, vol. 34, no. 4, pp. 2070–2083, Dec. 2019.

[33] S. Wang and F. C. Lee, "Investigation of the transformation between differential-mode and common-mode noises in an EMI filter due to unbalance," *IEEE Trans. Electromagn. Compat.*, vol. 52, no. 3, pp. 578–587, Aug. 2010.

[34] B. Wunsch, T. Christen, S. Skibin, and V. Forsstrom, "Broadband circuit model of a ferrite core, including dimensional resonance, saturation, and hysteresis," *IEEE Trans. Magn.*, vol. 55, no. 7, Jul. 2019, Art. no. 7300605.

[35] P. Papamanolis, "Optimal design of HF inductors and universal EV charger mains interfaces," PhD thesis, ETH Zurich, 2021.

[36] J. Kennedy and R. Eberhart, "Particle swarm optimization," in *Proc. Int. Conf. Neural Networks*, 2018, vol. 4, no. 2, pp. 1942–1948.

[37] CISPR17:2011, "Methods of measurement of the suppression characteristics of passive EMC filtering devices," 2011.

[38] C. D. Palacios, P. G. Vizuete, M. A. M. Prats, and J. Bernal-Méndez, "Smart shielding techniques for common mode chokes in EMI filters," *IEEE Trans. Electromagn. Compat.*, vol. 61, no. 4, pp. 1329–1336, Aug. 2019.

[39] A. Ojeda-Rodríguez, C. Domínguez-Palacios, J. Bernal-Méndez, and M. A. Martín-Prats, "Supplementary results of a theory for analyzing and characterizing common mode chokes for three phase systems," Jul. 2023. [Online]. Available: https://doi.org/10.6084/m9.figshare.23798559

[40] S. Wang, F. Lee, D. Chen, and W. Odendaal, "Effects of parasitic parameters on EMI filter performance," *IEEE Trans. Power Electron.*, vol. 19, no. 3, pp. 869–877, May 2004.

[41] P. Gonzalez-Vizuete, J. Bernal-Méndez, M. J. Freire, and M. A. Martin-Prats, "Improving performance of compact EMI filters by using metallic and ferrite sheets," *IEEE Trans. Power Electron.*, vol. 36, no. 8, pp. 9057–9068, Aug. 2021.

[42] D. E. Bockelman and W. R. Eisenstadt, "Combined differential and common-mode scattering parameters: Theory and simulation," *IEEE Trans. Microw. Theory Tech.*, vol. 43, no. 7, pp. 1530–1539, Jul. 1995.

[43] W. Fan, A. Lu, L. L. Wai, and B. K. Lok, "Mixed-mode s-parameter characterization of differential structures," in *Proc. 5th Electron. Packag. Technol. Conf.*, 2003, pp. 533–537.

[44] J. Brewer, "Kronecker products and matrix calculus in system theory," *IEEE Trans. Circuits Syst.*, vol. 25, no. 9, pp. 772–781, Sep. 1978.

[45] D. Pozar, *Microwave Engineering*. Hoboken, NJ, USA: Wiley, 2011.